CanmetMATERIALS

Finite Element Analysis of Tank Car Hard Coupling

GCDOCS Workflow ID 69534606

Submitted to Transport Canada

By

Jonathan McKinley, Jia Xue, Bruce W. Williams, Su Xu, and Mark Gesing

2021

TP Number: TP 15512E

ISBN Number: 978-0-660-41612-0

Catalogue Number: T44-3/27-2022E-PDF

CanmetMATERIALS

CanmetMATERIALS

DISCLAIMER

Natural Resources Canada makes no representations or warranties respecting the contents of this report, either expressed or implied, arising by law or otherwise, including but not limited to implied warranties or conditions of merchantability or fitness for a particular purpose.

CanmetMATERIALS

CanmetMATERIALS
GCDOCS Workflow ID

Finite element analysis of tank car hard coupling

By
Jonathan McKinley, Jia Xue, Bruce W. Williams, Su Xu and Mark Gesing

SUMMARY

A full-scale tank car FE model was developed, validated and used to simulate hard coupling impact. The material model used in the FE model was based on existing extensive testing of TC128B at various temperatures and strain-rates previously conducted by CMAT. It should be noted that this analysis is based on the assumption that the stub-sill is in an ideal condition with no embedded flaws in the structure.

Select hard coupling test results from the US DOT Federal Railroad Administration (FRA) were used to calibrate and validate the FE model. These FE analysis results agree well with the test results. In the worst scenario tested by FRA (10 mph, full on full, steel friction draft gear), the recorded peak load is above 1500 kips; and no significant plastic deformation and damage was observed at both ambient temperature and low temperature (-40 ^{o}C). Section 10.7 of the *Transportation of Dangerous Goods Regulations* limit coupling speeds to under 9.5 mph (15.3 kph), which is below the speed simulated here.

Locations of high stress concentration were identified and will be very helpful for future damage tolerance analysis (critical crack size). To optimize modelling resources and still accurately capture the influence of high stress regions, first a coarse mesh is used in full-scale simulations, and then a sub-model with a fine mesh is used to further model areas of high stress concentrations. This two-step strategy is found to be accurate and very efficient, which lays the foundation for future research.

Only minor plastic displacement and no damage initiation was found in the scenarios investigated in this research. As the FE model was developed to capture crack initiation and propagation, more aggressive loading conditions on the full-scale tank car may be explored in future research. This includes studying the influence of offset loading and embedded flaws. For instance, the vertical coupling force is also found to be important, which could cause the embedded flaws to open at the event of hard coupling. Additionally, the failure model employed in FE analysis was based on TC128B. Limited mechanical tests were done on A572-50, a common stub sill material, and compared to TC128B, which showed that the existing models for TC128B are adequate. Instead, future work should consider a failure model in FE analysis based on the TC128B weld material, as it has been shown that TC128B weld material fails at much lower energy than TC128B at the tested low temperatures between -20 ^{o}C and -80 ^{o}C.

The effect of low temperature at -40 ^{o}C and embedded flaws is briefly investigated in this research. The most severe scenarios with combined effect of low temperature and embedded flaw is recommend for future research. Future research could focus on investigating the combining effect of (1) fracture mode transition at low temperature, (2) pre-existing flaws, and (3) vertical coupling force.

LIST OF ABBREVIATIONS

CVN	Charpy absorbed energy
DOT	Department of Transportation (United States)
E.L.	Elongation
FEA	Finite Element Analysis
FE	Finite Element
FRA	Federal Railroad Administration (United States)
HAZ	Heat affected zone
LCF	Longitudinal coupling force
MMC	Modified-Mohr-Coulomb model
PEEQ	Equivalent plastic strain
R.A.	Reduction of area
RD	Rolling direction
RT	Room temperature
TC	Transport Canada
TD	Transverse direction
TDG	Transportation of Dangerous Goods
TSB	Transportation Safety Board of Canada
USDFLD	User defined field subroutine for implicit analysis
UTS	Ultimate Tensile Strength
VCF	Vertical coupling force
VUMAT	User defined material subroutine for explicit analysis
WM	Weld metal
XFEM	Extended finite element method
YS	Yield Strength

LIST OF SYMBOLS

α, m	Material constant for the damage model; damage evolution
C_1, C_2, C_3	Material constants for the damage model; damage initiation
ε	Strain
ε^p	Plastic strain
ε_f	Damage initiation strain
E	Modulus of Elasticity
D	Real time damage value
D_0	Damage initiation value
D_c	Critical damage value
σ_y	Yield Stress
σ_u	Ultimate Tensile Stress
σ	Stress
T	Temperature
t	Time
$\bar{u}_f^{pl}$	Material constant for the damage model; failure displacement
η	Stress triaxiality
θ_L	Normalized Lode angle
ϖ	Modelling parameter to control the softening of damaged elements

TABLE OF CONTENTS

1 INTRODUCTION

1.1 Background

In previous research, CanmetMATERIALS (CMAT) conducted a literature study on hard coupling of tank cars carrying dangerous goods in Canada. Section 10.7 of the *Transportation of Dangerous Goods Regulations* specifies maximum allowable impact velocities based on tank car weight and ambient temperature. The National Research Council conducted FE analysis of a tank car to identify the stub-sill as the area most likely to be damaged by hard coupling in the 1990s [1]. Due to the limitation of the time, the finite element analysis was a static linear elastic analysis that did not include either dynamic effects or an analysis of material failure or damage [2].

More recent studies have confirmed that common tank car materials such as TC128B do become brittle at low temperatures [3]. Although the hard coupling regulations do address this issue by reducing the allowable impact speeds from 12 kph (7.5 mph) at ambient temperature to 9.6 kph (6 mph) below -25°C for combined coupling mass above 150,000 kg, no data or analysis was found to support the specific temperatures and speeds used. Consequently, the current work included a research area of material temperature dependence.

Recent work by the FRA has shown great advancement in full scale testing and nonlinear dynamic analysis of tank cars in impact scenarios [4–8]. Although the analysis work focused on side and head impacts many of the techniques used can be adapted to hard coupling.

Since the previous linear FE analysis study [1], there has been many advancements particularly related to computational resources, material modeling and finite element simulation of tank cars that can be incorporated into car coupling analysis. This work used the nonlinear finite element analysis software ABAQUS and focused on developing the finite element model with the latest modelling techniques and updated material models to investigate the event of tank car hard coupling. The test data from the hard coupling tests performed by the FRA [9,10] were used to calibrate and validate the finite element models. The effect of low temperature and embedded flaws were also briefly investigated in this research.

1.2 Reviews of the recent FE analysis impact studies

Two recent reports by FRA, “Yard impact test of a tank car” (Short report, Aug 2019) [9] and “Impact Test Data Analysis for Load Environment Characterization of Tank Car Stub Sill During Yard operations” (Full report, March 2020) [10] were reviewed. The objective of the two reports was to characterize the coupling loads and the resulting strains in the stub sill of tank cars during yard operations. Seven hundred impact tests simulating various coupling conditions were conducted. The recorded data includes the tank car acceleration, coupler forces, impact speed, and strains at different locations on test cars. Among all the recorded data, the coupler forces and the corresponding strains are of great interests to our current research to simulate the hard coupling incidents through structural finite element analysis. The recorded coupler forces as shown in Figure 1 can be used as inputs for the newly developed finite element models.

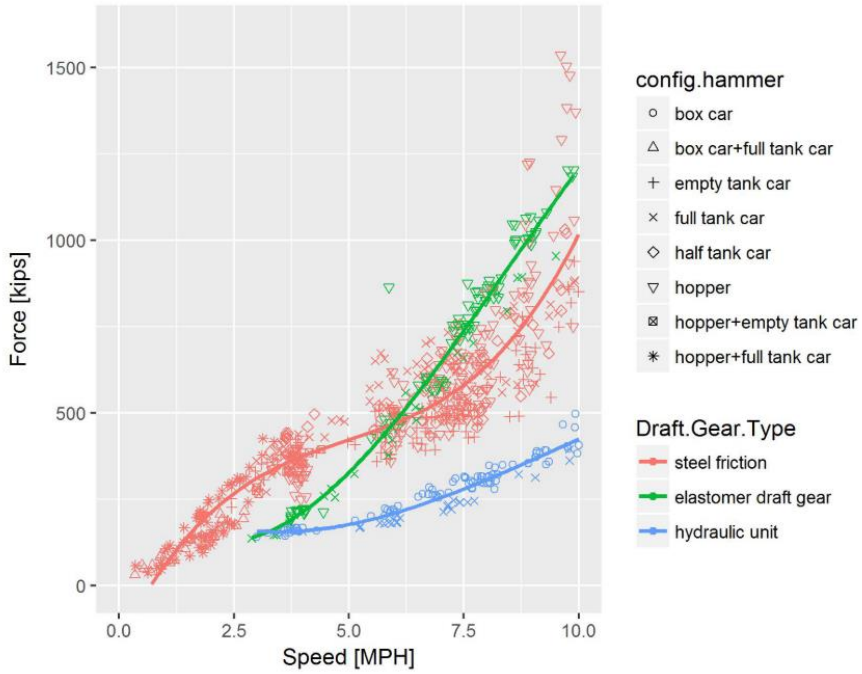

Figure 1: Coupler force versus speed for all impact tests conducted by the FRA [10]

The strains recorded at different locations on the test car are shown in Figure 2. Selected cases were used to calibrate and validate the finite element models presented in this report.

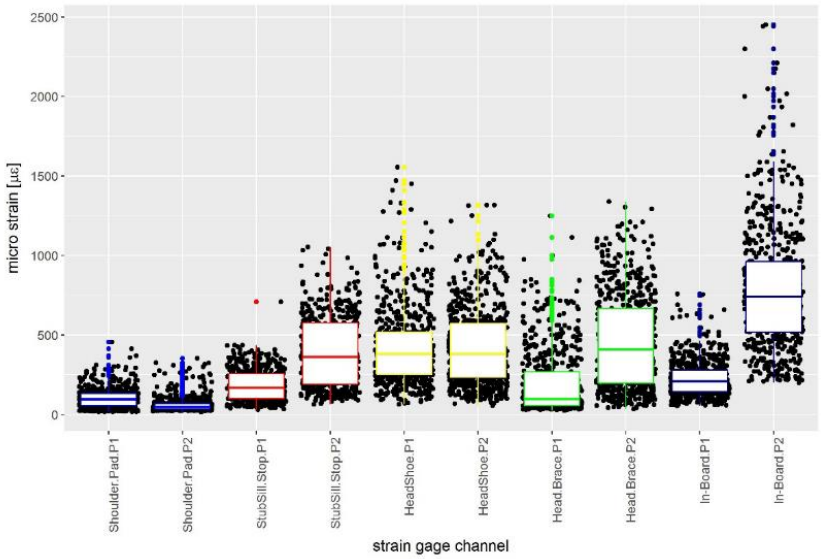

Figure 2: Boxplot comparison of principal strains throughout test program at different locations on test car courtesy of the FRA [10]

1.3 Establishment impact scenarios

Some of the test data was provided by FRA through Transport Canada, which was used to calibrate and validate the finite element models. The twenty-four received test data files can be divided into

eight scenarios with three repeats for each scenario, as listed in Table 1. Each scenario was repeated three times. The limited test scenarios and results discussed in this report are a small subset of the FRA tests. Full details on hard coupling tests and the detailed discussions regarding the relations between coupling speed and coupling forces can be found in the FRA report[10].

Table 1: Details of the impact scenarios used to calibrate and validate FE models

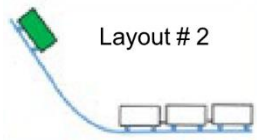

Sceinarios	Layout	Hammer car	Anvil Car	Speed	Draft gear type
1	#2	Empty	Full	6 mph/9.66 kph	901E steel friction
2	#2	Empty	Full	10 mph/16.09 kph	901E steel friction
3	#2	Partially Full	Full	6 mph/9.66 kph	901E steel friction
4	#2	Partially Full	Full	10 mph/16.09 kph	901E steel friction
5	#2	Full	Full	6 mph/9.66 kph	901E steel friction
6	#2	Full	Full	10 mph/16.09 kph	901E steel friction
7	#2	Full	Full	6 mph/9.66 kph	901G TwinPack
8	#2	Full	Full	10 mph/16.09 kph	901G TwinPack

The test data was recorded on 27 channels, which are listed below in Table 2. The test data includes tank car acceleration, coupler forces and strains at various locations. The coupler forces will be used as input for the finite element model and the strain readings will be used to compare with the simulation results.

Table 2: Recorded data for each scenario

Channel #	Recorded data
1	Car body Acceleration Longitudinal
2	Car body Acceleration Vertical
3	Car body Acceleration Lateral
4	Stub Sill Acceleration Vertical B-end
5	Stub Sill Acceleration Longitudinal B-end
6	Stub Sill Acceleration Lateral A-end
7	Stub Sill Acceleration Vertical A-end
8	Axlebox Acceleration Vertical A-end Right
9	Stub Sill Acceleration Longitudinal A-end
10	Long Coupler force A-end
11	Long Coupler force B-end
12	Shoulder Pad Rosette +45
13	Shoulder Pad Rosette Vertical
14	Shoulder Pad Rosette -45
15	Vertical Coupler force A-end
16	Stub Sill-draft stop- Rosette Longitudinal
17	Stub Sill-draft stop- Rosette 45

18 Stub Sill-draft stop- Rosette Vertical
19 Head Shoe Rosette Longitudinal
20 Head Shoe Rosette 45
21 Head Shoe Rosette Vertical
22 Head Brace Rosette Longitudinal
23 Head Brace Rosette 45
24 Head Brace Rosette Lateral
25 In-Board Rosette Longitudinal
26 In-Board Rosette 45
27 In-Board Rosette Lateral

Figure 3 shows the installed coupler instrumented with strain gauges. According to the report, longitudinal force bridges on the instrumented couplers, were calibrated in a laboratory prior to installation on the vehicle. The coupler force in the data files are taken to be determined from strains of the couplers. The strain-to-force conversion was not indicated, and therefore the coupler calibration was conducted using the FE analysis predicted results.

Figure 3: Instrumented coupler for measuring longitudinal coupler forces used by the FRA[10]

A-end (striking end) and B-end (non-struck end) of the tank car should have similar coupler force according to the report, however the recorded strain magnitude from the two couplers are very different, as shown in Figure 4 (a). The assumption is that the strain gauges were attached in different locations of the couplers making the strain-to-force conversion very different for these two couplers. More strain gauges were attached to the A-end than the B-end. Coupler strain data from A-end of the tank is used as inputs in this research. The recorded vertical coupler strain is generally very low when compared with the longitudinal coupler strain as shown in Figure 4 (b) and therefore vertical coupler force is not included in the current FE analysis. The vertical coupling forces were much lower than the horizontal forces and the level of noise was quite high. It was therefore difficult to filter and calibrate the data effectively. Vertical coupler forces may be considered in future work.

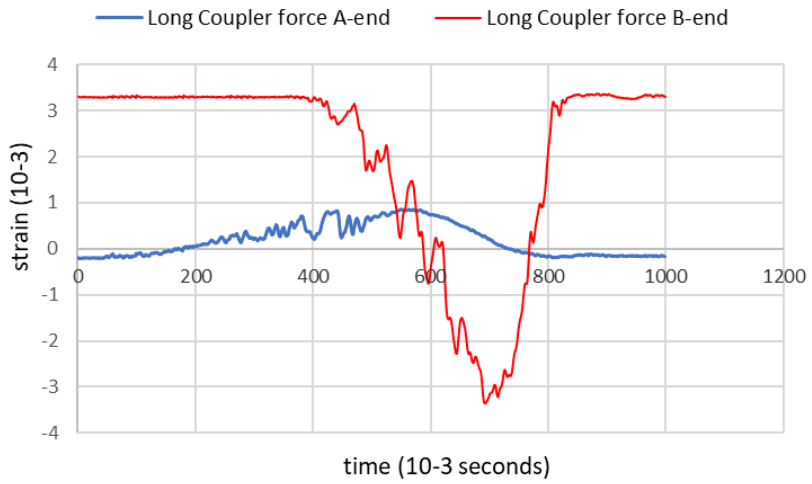

(a)

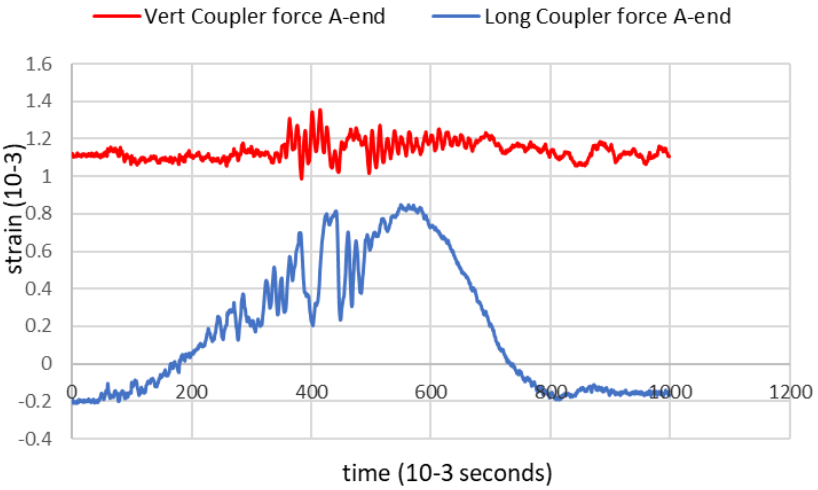

(b)

Figure 4: Recorded longitudinal and vertical coupler strain for scenarios 5

The raw strain data was recorded at the frequency of 10 kHz, which is too noisy to be directly input into the finite element model. The received test data were filtered and smoothed using the program Origin before use in the simulations. A low pass filter with frequency of 0.01 Hz was first used to remove the noises from the raw test data, as shown in Figure 5 (a). Low-pass filters block all frequency components above the cutoff frequency, allowing only the low frequency components to pass. The filtered data have about 1000 data points, which is further smoothed and reduced to about 50 data points, which is more suitable to be used as FE analysis inputs. When the same low-pass filter is applied to the vertical coupler strain, the filtered vertical coupler strain curve is almost flat and it's assumed that the vertical coupler force is relatively too low and therefore not considered in current simulations. The processed longitudinal coupler strain-time curve was then scaled to force-time curves based on the peak coupler force reported in the FRA report, which is about 2,224 kN (500 kips) for scenario 5. The final coupler force-time curve that was used as inputs for FE analysis is shown in Figure 5 (b).

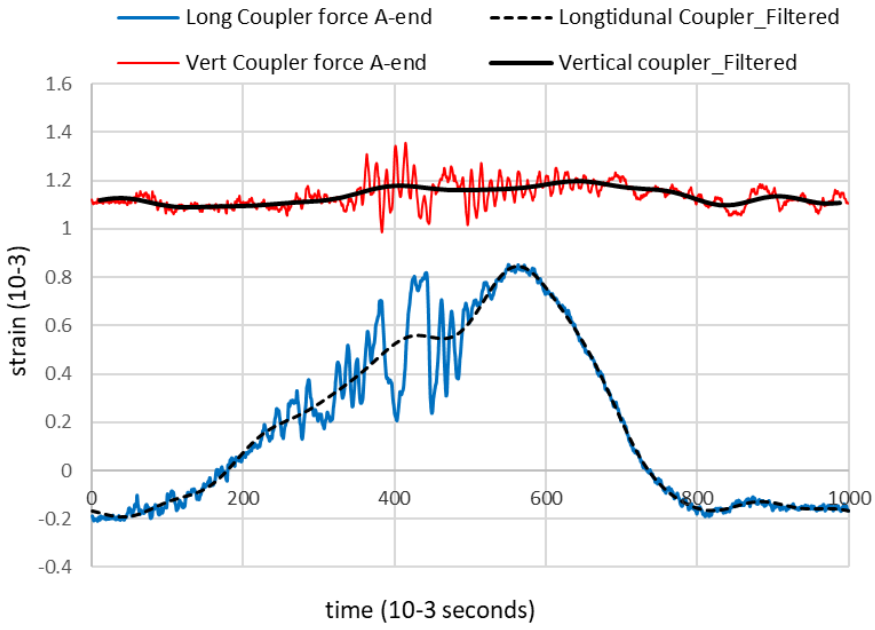

(a)

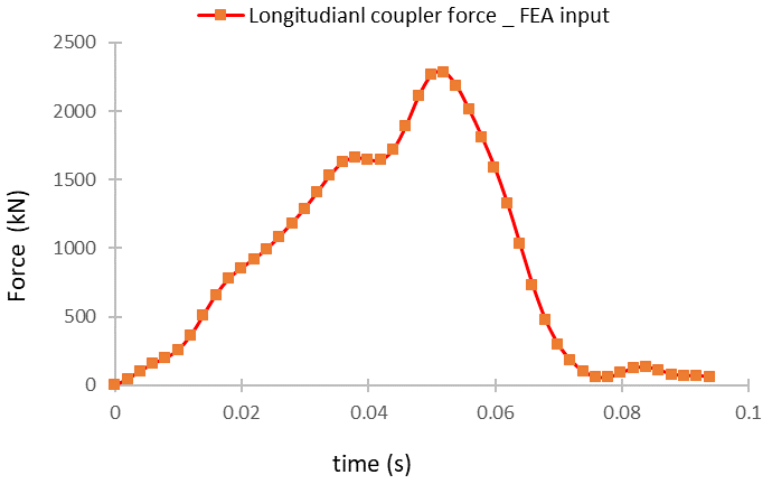

(b)

Figure 5: Processing of raw strain data to be used as inputs for FE analysis

2 FINITE ELMENT ANALYSIS AND RESULTS

The non-linear material model used in CMAT's FE analysis considered both elastic and plastic deformation of TC128B steel. The model was also able to capture both crack initiation and propagation in small scale validation experiments, with crack initiation being most relevant to hard coupling. In metal, a few mechanisms for crack formation including void nucleation, growth, and coalescence, fatigue crack initiation, and environmentally-assisted-cracking (which includes stress-corrosion-cracking). Fatigue crack initiation occurs by an accumulation of damage at the micro-scale in the material. Fatigue crack initiation, which can occur below the yield strength of the material, was not explored in the current work but could be considered if repeated hard coupling events are of concern. The void nucleation, growth, and coalescence mechanism is applicable to a ductile metal and was described using a damage mechanics model. Consideration was also given to brittle, or cleavage, fracture which occurs at low temperatures. The literature review of hard coupling conducted by CMAT did not identify environmentally assisted cracking as a concern for hard coupling.

2.1 Damage mechanics model

There are generally two parts to damage models that define the fracture surface of the material; damage initiation and damage evolution. The Modified-Mohr-Coulomb (MMC) model detailed in [11] was used to model damage initiation. In this model, the strain to initiate fracture, ε_f, depends on stress triaxiliaty, η, and Lode angle, θ_L. Triaxiality is a single parameter that describes the degree of influence of hydrostatic stress in a given three-dimensional stress state. The Lode angle is another measure of the three-dimensional stress state. It is a measure of the applied ratio of the three principal stresses. For the same triaxiality, varying the principal stresses will either increase or decrease the void nucleation, growth, and coalescence rate which influences the failure response of ductile metals. The influence of Lode angle is largest in shear, which is why it is often associated with shear deformation.

The damage initiation strain is given by

$$\varepsilon_f = \left\{\frac{A}{C_2}\left[C_3 + \frac{\sqrt{3}}{2-\sqrt{3}}(1-C_3)\left(sec\left(\frac{\theta_L\pi}{6}\right)-1\right)\right]\left[\sqrt{\frac{1+{C_1}^2}{3}}cos\left(\frac{\theta_L\pi}{6}\right) + C_1\left(\eta + \frac{1}{3}sin\left(\frac{\theta_L\pi}{6}\right)\right)\right]\right\}^{-1/n} \quad (1)$$

with C_1, C_2, and C_3 being material constants for a specific temperature and strain-rate. Damage increases according to:

$$D = \int_0^{\varepsilon^p} \frac{1}{\varepsilon_f} d\varepsilon^p \quad (2)$$

with damage initiation occurring at a value of unity. After initiation, the damage evolution criterion describes the softening of the element. Paredes et al. [12] used the MMC model for damage initiation with the following damage evolution criterion:

$$\varpi = \left(\frac{D_c - D}{D_c - D_0}\right)^m \tag{3}$$

As the damage, D, is a function of stress triaxiality and Lode angle, so too is damage evolution. Paredes et al. discussed that upon damage initiation at D_0=1 softening evolves until D_c, the critical damage value, at which final fracture occurs (equivalent to deleting the element in an FE simulation) with m being a material constant. An alternative criterion for damage evolution is given by:

$$\varpi = \frac{1 - \exp\left(-\alpha \dfrac{\bar{u}^{pl}}{\bar{u}_f^{pl}}\right)}{1 - \exp(-\alpha)} \tag{4}$$

where α and $\bar{u}_f^{pl}$ are material constants for a given temperature and strain-rate. This equation is not a function of stress triaxiality and Lode angle. This is the form of damage evolution that was used in ABAQUS for the implicit simulations, with the value for $\bar{u}^{pl}$ being computed by the software. Future work should consider the role of the damage evolution criterion on the transition from flat to slant fracture, as it was not studied in the current work.

To calibrate the MMC damage initiation parameters, Paredes et al. performed a number of mechanical tests on TC128 steel [13], which included tensile, notched round bar, biaxial and shear tests, and tests on flat specimens with circular cut-outs. These tests were required to produce a range of triaxiality and Lode angles for accurate model calibration. In additional to mechanical testing, several FE analysis were carried out to calculate parameters such as stress triaxiality and Lode angle for the various specimen geometries. An optimization process was used to minimize the error between simulations and experiments during model calibration. In the current work, the MMC surface was described using the damage initiation routines available in ABAQUS. The damage initiation surface used in this research is shown in Figure 6.

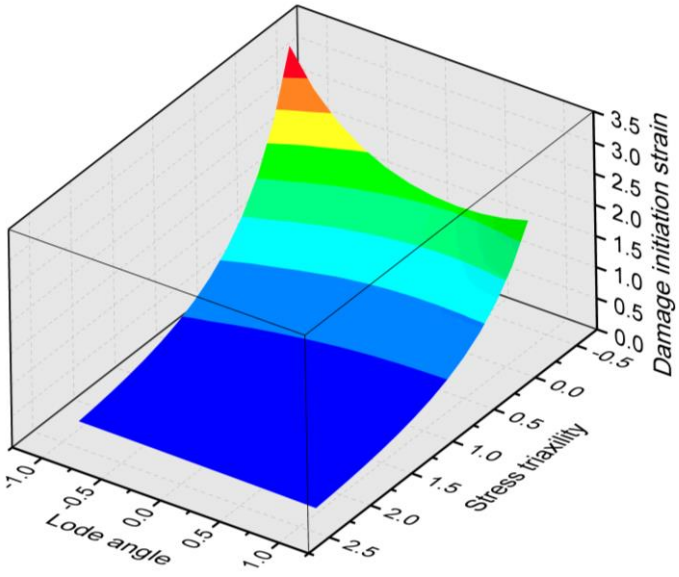

Figure 6: Damage initiation strain defined as a function of stress triaxiality and normalized lode angle

In the work of Paredes et al. [12–14], the softening of the element was described using a non-linear relationship which was also dependent on triaxiality and Lode angle (Equation 3). In the current work, the built-in damage evolution law in ABAQUS (Equation 4) was used to control the softening of damaged elements and was based on linear softening for which stability was maintained with the implicit solver.

A damage mechanics model with the MMC criterion was used in FE analysis to describe the failure response of TC128B for temperatures ranging from 24 °C to -80 °C under quasi-static and dynamic strain-rates. Previously [15], it was shown that the model could accurately predict the ductile fracture response of Charpy V-Notch (CVN) specimens for TC128B. However, the MMC could not predict the sudden load drop that occurred due to brittle (cleavage) fracture at low temperatures. In the current work, the FE model was extended to account for brittle fracture using a maximum principal stress criterion. The failure model was fully detailed in [16] with only brief details given in this current report. The ductile only versus ductile-brittle load responses predicted from CVN simulations is compared in Figure 7 for TC128B at -40 °C along with the measured response. Figure 7 (b) shows that load drop due to brittle fracture was accurately predicted when preceded by ductile crack growth.

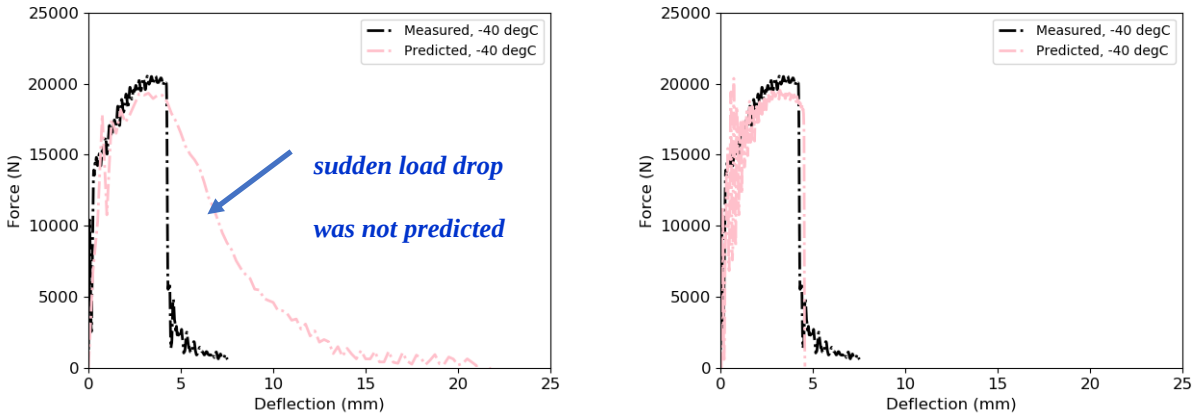

Figure 7: Predicted versus measured load response from Charpy specimens for TC128B at -40 °C a) ductile only model and b) ductile-brittle model [16]

The model detailed in [16] was implemented in the explicit FE analysis software DYNA3D as a user defined subroutine. The tank car simulations outlined in this report were performed using ABAQUS. Consequently, the material model was implemented as a user defined subroutine in the explicit FE analysis framework, or VUMAT, in ABAQUS. Comparison of the Charpy load responses predicted between the two software for TC128B from 24 °C to -80 °C along with the measured responses are shown in Figure 8. The DYNA3D and ABAQUS subroutines produced very similar responses. Slight differences were attributed to small variations in how the subroutines were implemented in the software.

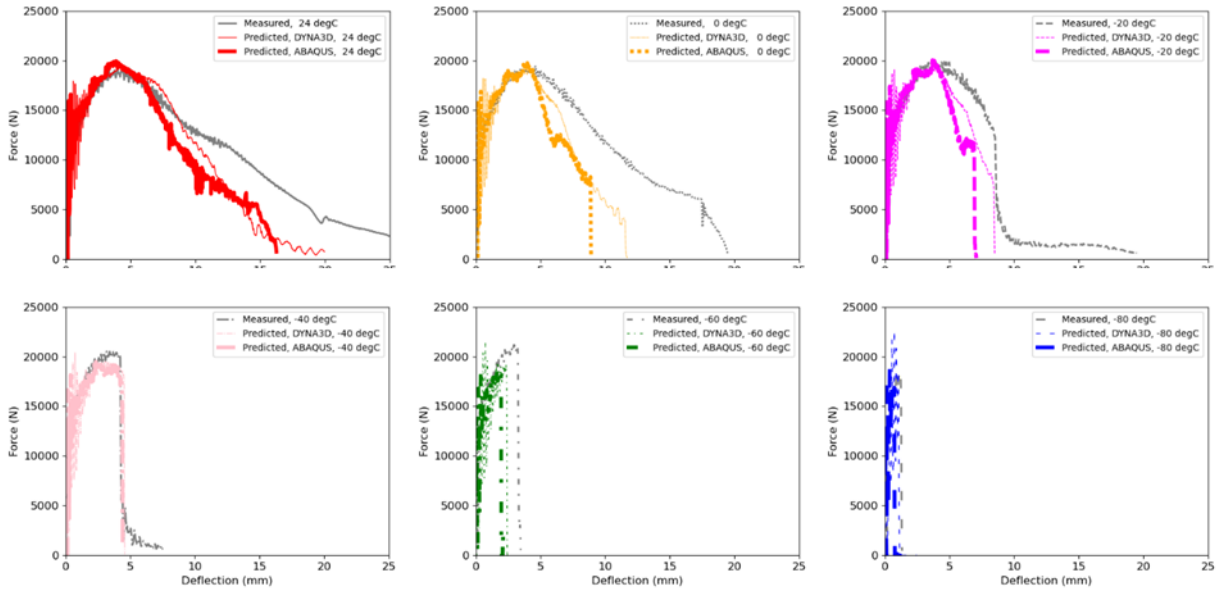

Figure 8: Charpy load response comparison between DYNA3D and ABAQUS damage models, along with measured responses for TC128B with temperatures from 24 °C to -80 °C [16]

As with many other metals, damage models have been recently adopted and used in FE analysis to describe the failure response of tank car steel as reported by Kirkpatrick and McKeighan [17], Przemyslaw et al. [18], and Eshraghi and Carolan [19]. It is important to emphasize that damage model coefficients are mesh dependant. In the current work, the damage model coefficients were calibrated and validated based on a mesh size of 0.2 mm. However, the large-scale tank car simulations used a mesh size of about 10 mm. This difference was not expected to influence the current results due to low levels of plastic deformation. In future work, the various damage models proposed to describe the response of TC128B should be compared to isolate the influence of mesh size if plastic deformation is predicted. Though the damage model based on a 0.2 mm mesh size was applied to the large-scale FE model, it did not influence the results in this work as no or little plastic deformation and damage occurred. If plastic deformation is predicted then the sub-modelling technique can be applied at a more local scale and the mesh size can be refined as needed. Additionally, the lowest Charpy response has been measured in the weld material for TC128B. Consequently, it is recommended that a fracture model for the TC128B weld material be developed.

As mentioned above, the damage model was implemented as an explicit user subroutine in ABAQUS/Explicit. Alternatively, the damage routines already available in ABAQUS (using the keywords damage initiation and damage evolution) were employed. These routines were also applied in the implicit FE analysis framework using ABAQUS/Standard. The dynamic hard coupling simulations were simulated using the implicit dynamic solver in ABAQUS. An advantage to the implicit solver was that a much lower number of analysis steps to completion was required which reduced run-time compared to an explicit solver. A drawback of an implicit solver is the requirement for large memory for large FE models, which is less of an issue with current computation resources. Another drawback is that implicit simulations are less stable during crack propagation compared to an explicit solver. As crack propagation was not of major issue in the current tank car simulations, the implicit solvers in ABAQUS were used for the hard coupling

simulations detailed in this report. A ductile-brittle model was required for the low temperature (-40 °C) simulation. A simple implicit user subroutine (USDFLD) for brittle fracture was used for the low temperature simulation to ensure a sudden load drop could be predicted if the stress/strain were too large.

2.2 Updated tank car model

A structural model of a DOT-117 tank car was built using drawings provided by Transport Canada. The tank car model, which was initially built as a one-part shell, now consists of three parts, as shown in Figure 9. The sill (solid region) is connected to the sub sill (shell region) through shell-to-solid coupling. The tank shell and stub-sill are connected with tie constraints along weld lines. The welds are modeled using the same material properties as the base metal.

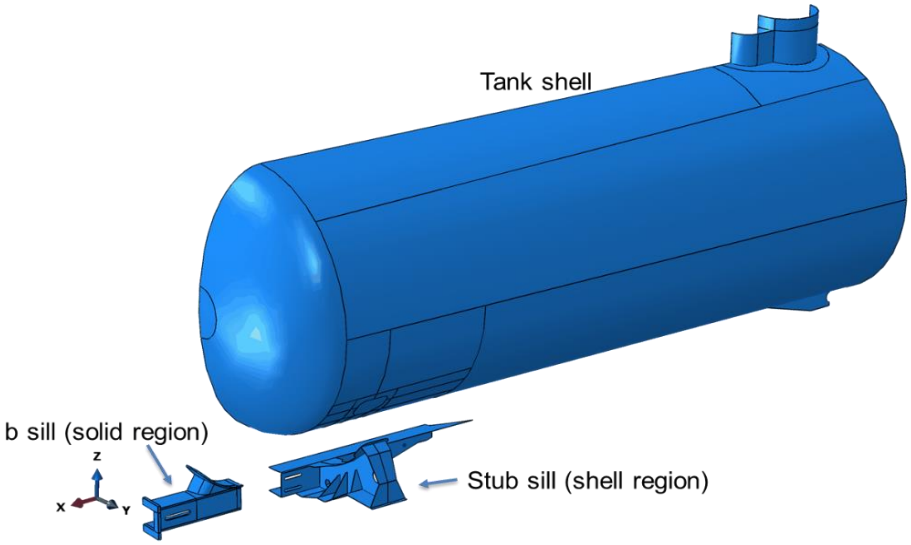

Figure 9: Updated tank car model consisted of three parts

The stub-sill solid region was reconstructed with more detailed partitions to improve mesh quality, and only hex elements are used for better accuracy during possible deformation and crack initiation. The solid region of the stub sill is expected to have higher stress/strain than the rest of the stub sill and thus a more refined mesh is used for this region. The detailed view of the solid region of the tank car stub sill is shown in Figure 10.

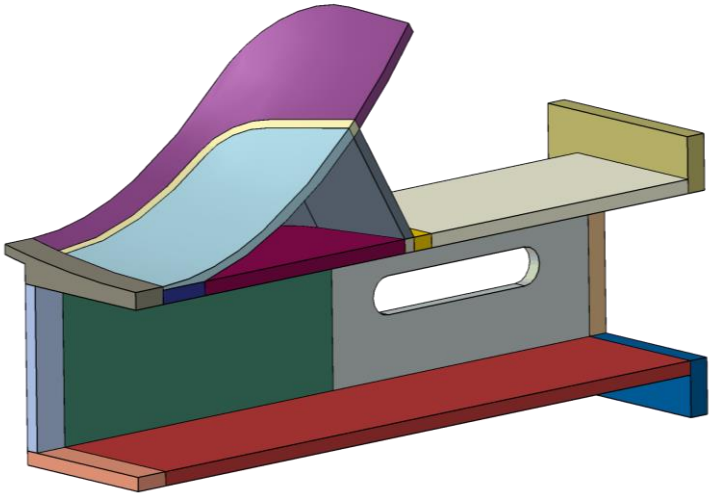

(a)

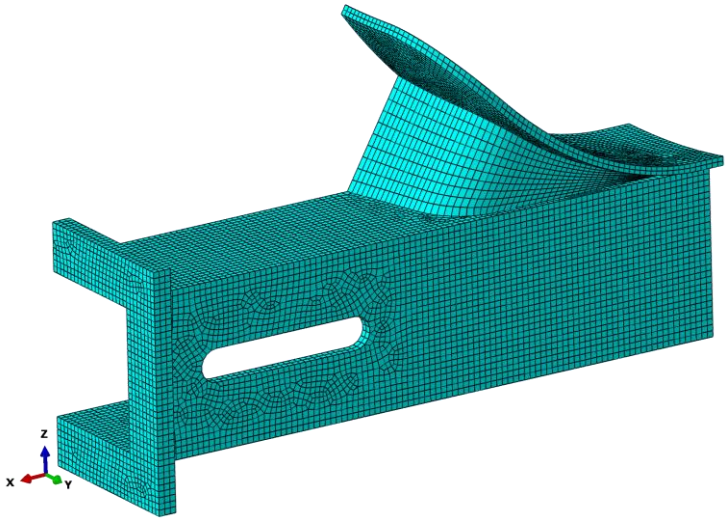

(b)

Figure 10: Partitions (a) and mesh (b) of the solid region of the tank car stub sill

The stub sill and the tank shell are connected with weld lines (tie constraints). No failure criterion was defined for the weld lines in this study. Contact constraint between stub-sill and tank shell was also defined to prevent mesh penetration. Weld lines are highlighted in red in Figure 11 below.

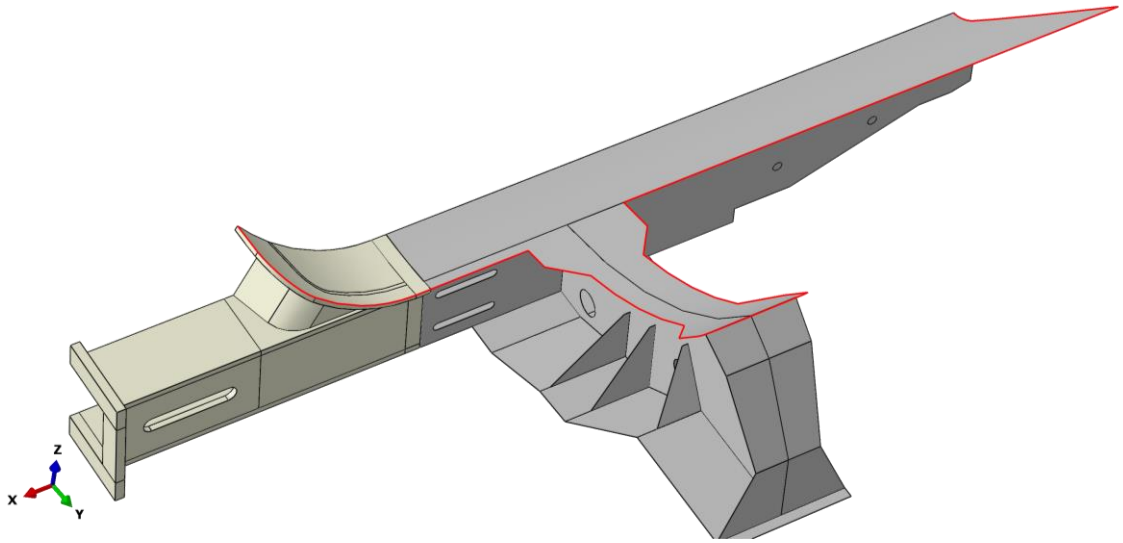

Figure 11: Stub sill with highlighted weld lines

The boundary condition of the tank car model is shown in Figure 12. A quarter symmetric model was used to reduce computation time. Rigid constraint of the tank car in vertical direction (Z) was later found to cause high stress concentration, and it was replaced with elastic constraint to simulate the effect of tank car suspension. The suspension of the tank car wheel assembly is simulated as an elastic spring element. The bottom surface of the stub sill is tied to one end of the spring element in the vertical direction, and the other end of the spring element is connected to the ground. The spring stiffness is assumed to be 100 kN/mm based on engineering judgement, which lead to spring displacement of 2.98 mm when the tank is filled with water. A two-step implicit analysis is used by default. The first step is an implicit static analysis to apply gravity load and the second step is a dynamic implicit analysis to apply coupler forces.

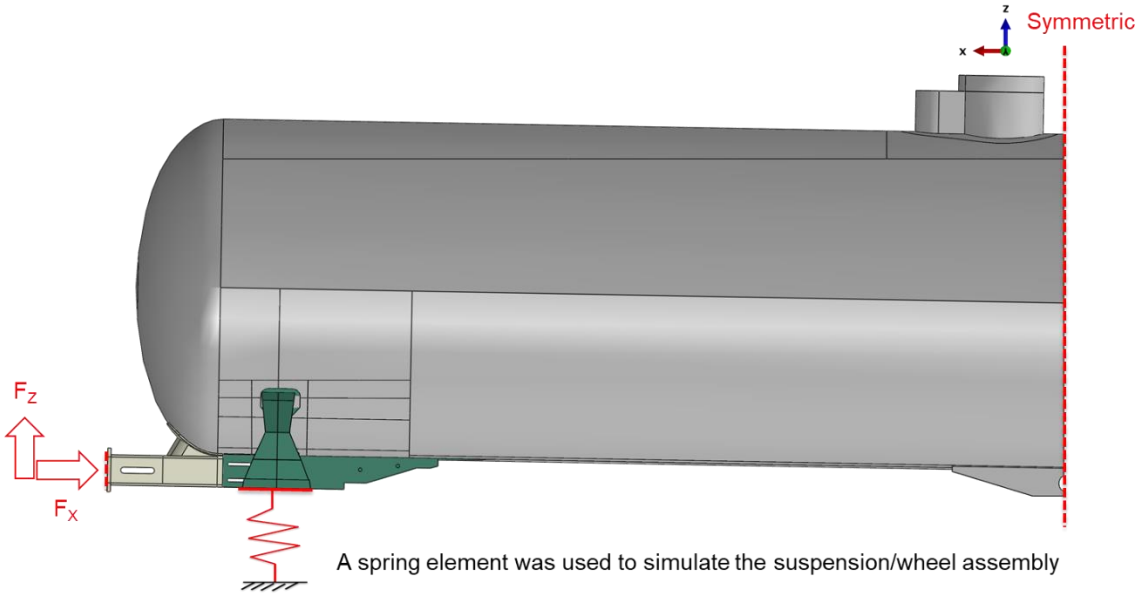

Figure 12: Boundary condition of the tank car model

For balanced efficiency and accuracy, a multi-scale meshing strategy was used. The majority of the tank and stub sill was meshed with 50 mm shell elements which are coarse but computationally efficient. Shell elements are usually used to model structures in which one dimension, the thickness, is significantly smaller than the other dimensions. Conventional shell elements use this condition to discretize a body by defining the geometry at a reference surface. In this case the thickness is defined through the section property definition [20]. Shell elements can be a huge time save since they allow the modelling of thin features with relatively much fewer elements than solid elements. Smaller 10 mm solid elements are used in areas that are expected to have higher stress concentrations to improve accuracy. As highlighted in red in Figure 13, a high (von Mises) stressed region can be found typically near the head brace.

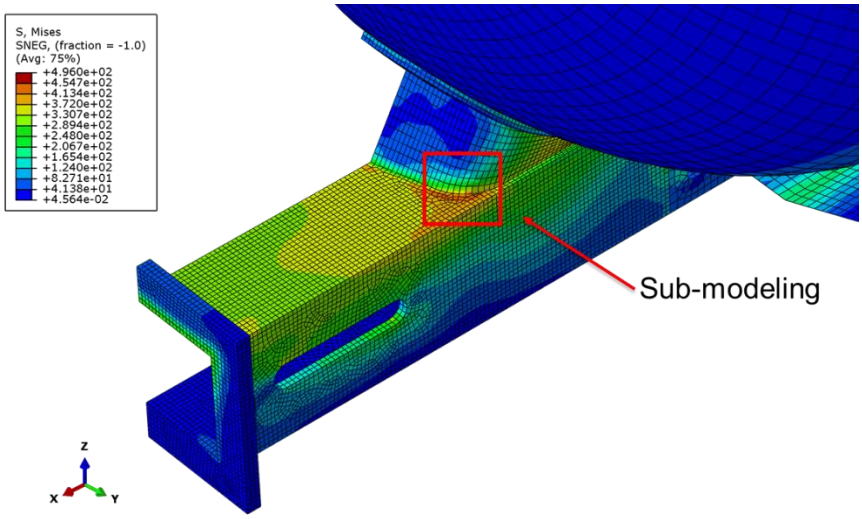

Figure 13: Relatively coarse mesh for the global model

The high stress concentration regions of the stub sill in the global model can be rebuilt as sub-models with further refined meshes for more accurate stress prediction. Node-based solid-to-solid sub modeling method was used to rerun the sub model of high-stress regions. The boundary conditions of the sub-model are read from the simulation results of the global model. Hex solid elements for in the sub model have a refined mesh size between around 2 mm for this case and it can be further refined to 0.2 mm if damage initiation was expected. This reduces the influence of mesh size effects. Our current damage models are calibrated at 0.2 mm mesh size. Sub modeled regions can be re-run without having to run the entire tank car model simulation.

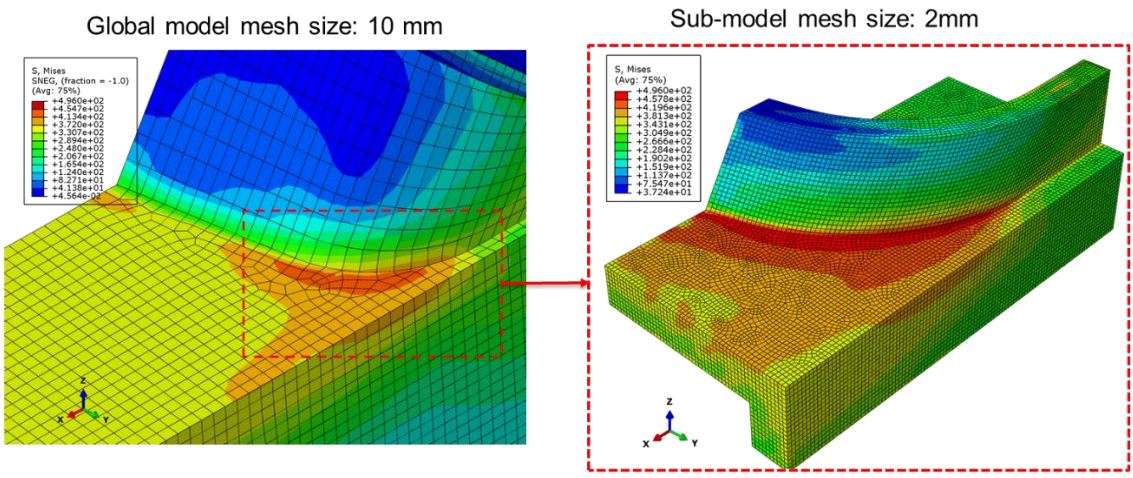

Figure 14: The high stress region in the global model (a) is rebuilt with finer mesh in the sub model (b).

2.3 Comparison of the modelling strategy

The FRA had conducted a significant amount of valuable research in the area of modelling tank car impact scenarios. Much of this work was instrumental to CMAT's hard coupling efforts such as publishing the damage models of TC128B [4,6,8,21–23]. There are also significant differences between the work that the FRA has done. These differences are summarised in Table 3.

Table 3: Comparison between FRA large deformation impact simulations and CMAT hard coupling simulations

	FRA	**CMAT**
Application/Failure mode	Side impact: puncture of tank shell large damage zone Large deformation (strain)	Hard coupling: relatively small cracks near the stub sill small damage zone Small deformations
FE analysis approach	Dynamic explicit analysis. One step analysis, full scale FE analysis with damage model. Sub modeling can't be used in the side impact analysis due to large damage zone)	Both dynamic implicit and explicit analysis can be used. Two step analysis with assumption that small cracks (small damage zone) have limited effect on global mechanical behavior. (1) Global stress analysis (2) sub-modeling with damage model
Boundary conditions	Complex boundary conditions involving moving impactor at	Simplified boundary conditions using experimentally measured coupler

	high speed and sloshing within the tank car.	force as inputs and no sloshing was considered for now.
Stress state	2D plane stress state at tank shell, mostly hoop and axial stress.	3D stress state at stub sill.
Failure criterion	2D fracture locus: PEEQ as a function of triaxiality.	3D fracture surface: PEEQ as a function of triaxiality and Lode angle.
Mesh size of the damage model	Around 2 mm, for the full-scale FE model of the tank car.	0.2 mm, for the detailed damage analysis with sub modeling.
Effect of low temperature	Not considered.	Damage model with ductile-to-brittle transition at low temperatures.
Effect of pre-existing flaws	Not considered. It's not practical to include flaws in the full scale FE model	Pre-existing flaws can be easily added in the sub model.

2.4 Comparison of FE analysis results and test data

The FRA impact test data was used to validate the finite element model. Eight cases were chosen to run in the finite element model to compare the predicted strain with the experimentally recorded data. Two locations, namely the "stub sill" and "in-board", in the tank car were found to have significant strain recorded during the hard coupling test, and thus these two locations were chosen to compare with the FE analysis predicted results. One location of interest is referred as the "stub sill" location, where strain gauges are installed on the stub sill close to the rear stop and the corresponding element in the finite element method is shown in Figure 15.

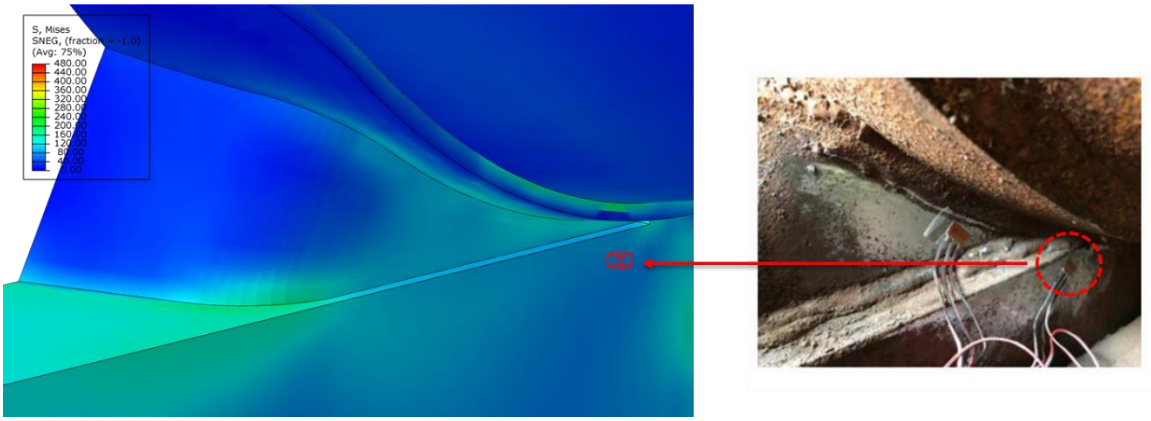

Figure 15: Strain gauge installed on the stub sill close to the rear stop and the corresponding element in the finite element model

The other location of interest is referred as the "in-board", where strain gauges were installed under the car at the end of the stub sill beam. One element best fit the description were chose in the finite element model to compare the strain results with test data. The "in-board" strain gauge and the corresponding element is shown in Figure 16.

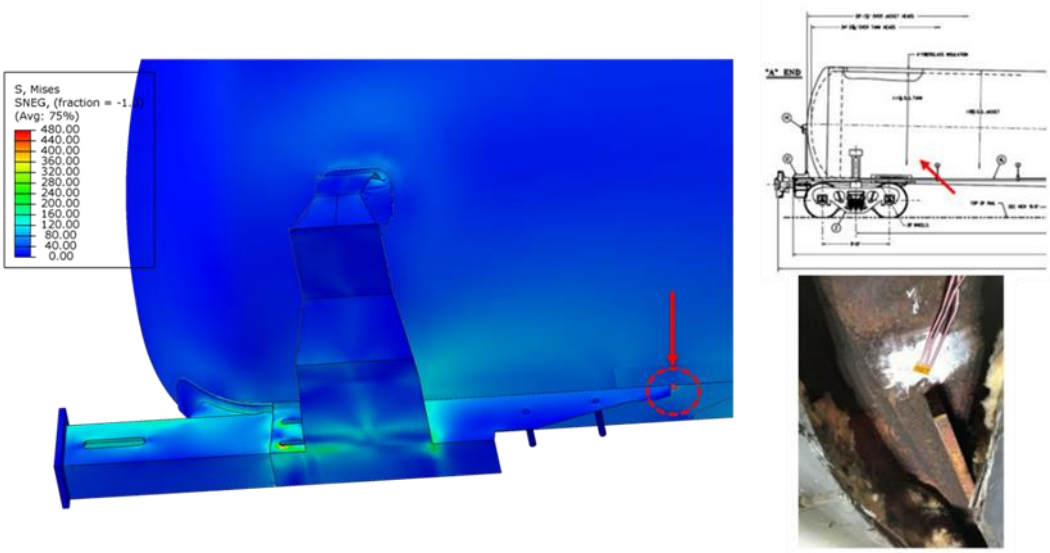

Figure 16: In-board strain gauge installed under the car at the end of the stub sill beam and the corresponding element in the finite element model

Case 5 was used to calibrate the conversion of recorded coupler strain to coupler forces, which can be used as inputs for the finite element. The coupler force for the Case 5 was calibrated to make sure the FE analysis predicted strain agree well with the tested data as shown in Figure 17.

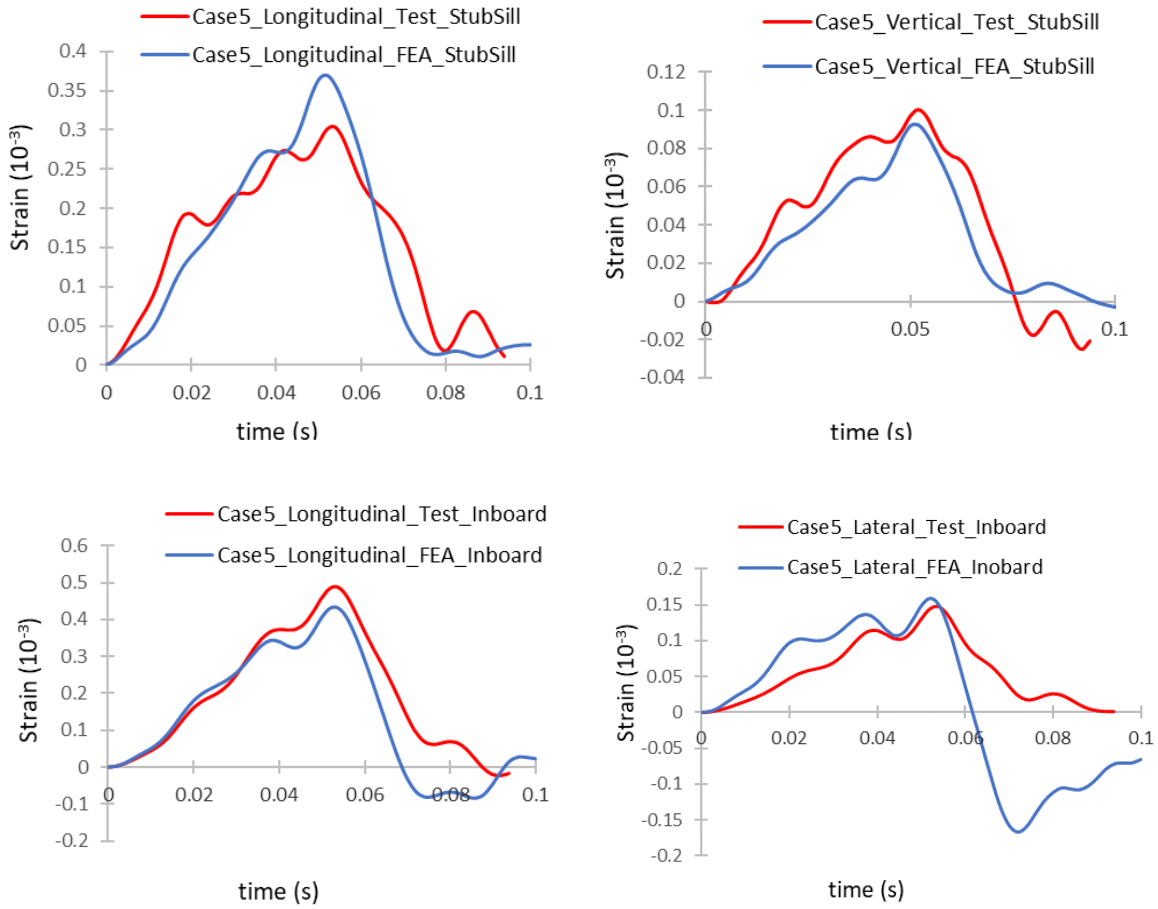

Figure 17: Comparions of experimental and predicted strain for case 5

The calibrated coupler strain-to-force conversion was used for case 1-4 and 6, which have the same configurations in terms of draft gear and coupler set up.

For cases 7 and 8, a different draft gear and coupler were used and thus the coupler strain-to-force conversion was recalibrated using the test data from case 7. The calibrated coupler strain-to-force conversion was used for case 8 for validation. Comparison of FE analysis and test results for all the remaining cases was shown in Figure 18. FE analysis results generally agree well with the test results.

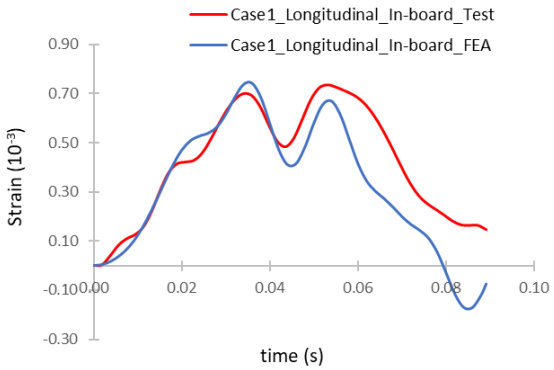
Case1_Longitudinal_In-board_Test
Case1_Longitudinal_In-board_FEA
Strain (10-3)
time (s)

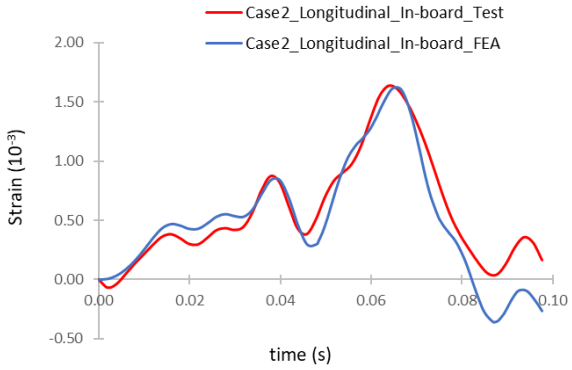
Case2_Longitudinal_In-board_Test
Case2_Longitudinal_In-board_FEA
Strain (10-3)
time (s)

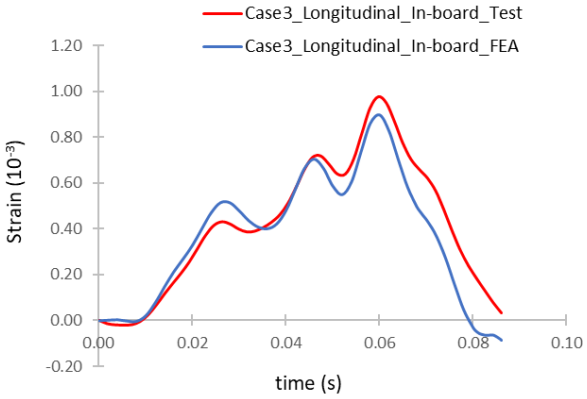
Case3_Longitudinal_In-board_Test
Case3_Longitudinal_In-board_FEA
Strain (10-3)
time (s)

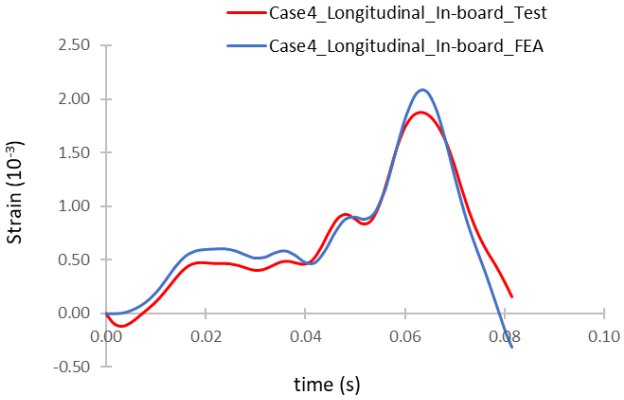
Case4_Longitudinal_In-board_Test
Case4_Longitudinal_In-board_FEA
Strain (10-3)
time (s)

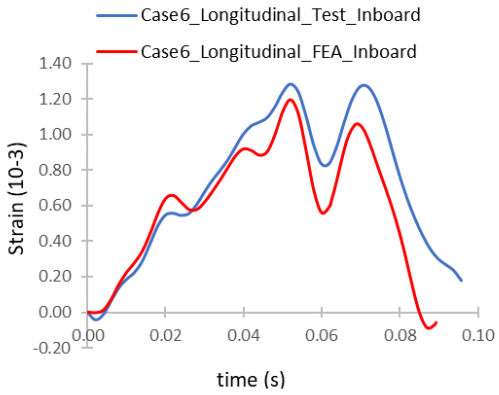
Case6_Longitudinal_Test_Inboard
Case6_Longitudinal_FEA_Inboard
Strain (10-3)
time (s)

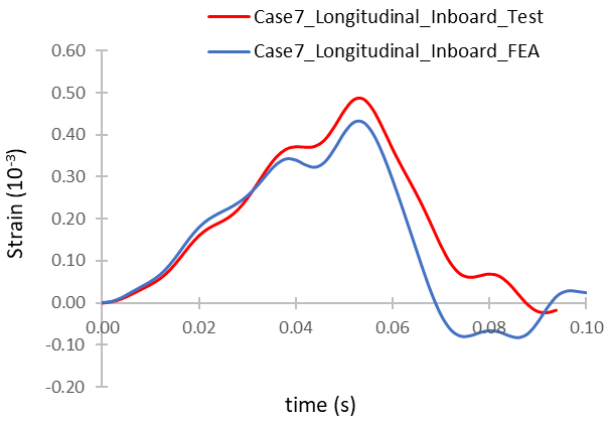
Case7_Longitudinal_Inboard_Test
Case7_Longitudinal_Inboard_FEA
Strain (10-3)
time (s)

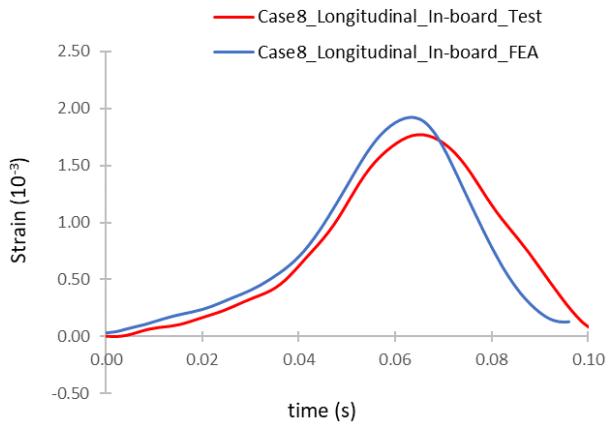

Figure 18: Comparions of experimental and predicted strain for the remaining cases

In this section, hard coupling test results from FRA were used to calibrate and validate the FE model. The model is found to be accurate and very efficient, which lays the foundation for future application of the model to more aggressive loading conditions. Only minor plastic displacement and no damage initiation was found in all the eight scenarios investigated in this research. The relatively more severe cases, such as case 2, 4, 6, and 8, have a coupling speed of 16.09 kph (10 mph), which is above the current coupling speed limit.

For example, Figure 19 shows the distribution of Von Mises stress and equivalent plastic strain for case 6. The distribution of the Von Mises stress is plotted at the peak load of 1,445 kips (6,428 kN), while the accumulated equivalent plastic strain is plotted at the end of simulation. High stress can be found near the interface between stub sill and tank shell as expected. High stress was also found near the lower slot in the stub sill, because the slot is in the load path and the opening caused stress concentration. Only minor plastic strain was found near the lower slot, and there is no noticeable plastic strain in the rest of the structure. It should be noted that quarter-symmetric boundary condition was used in this analysis, which is proved to be both accurate and computationally efficient.

It should also be noted that the peak load in this case is 1,445 kips (6,428 kN), which is above the design limit of 1,000 kips (4,448 kN), at which point some minor plastic deformation was not unexpected and some plastic strain can be observed in Figure 19 (b).

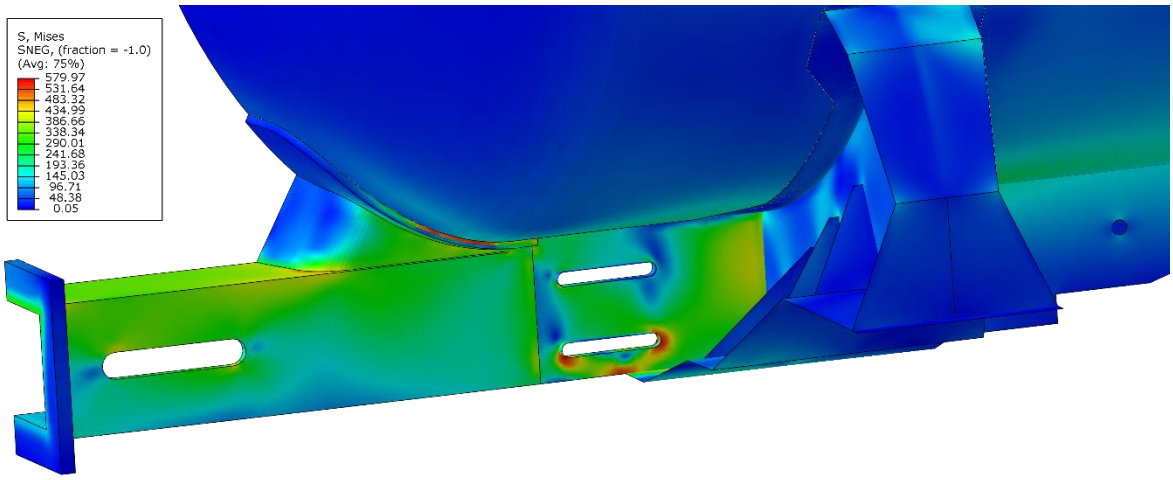

(a)

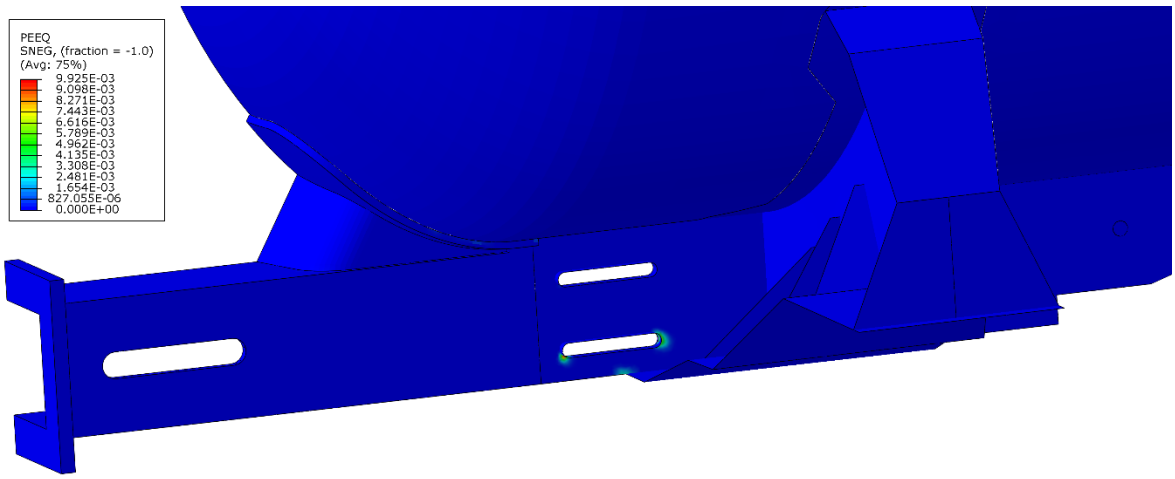

(b)

Figure 19: Distribution of Von Mises stress (a) and equivalent plastic strain (b) for case 6.

The smaller slots in the lower tank car sill were present in the drawings supplied to CMAT were not present in pictures of the tank car stub sill in the FRA reports as shown in the Figure 20, so the finite element model of case 6 with no slots in the lower stub sill was also investigated. Figure 21 shows the distribution of Von Mises stress and equivalent plastic strain for the modified case 6, which has no slots in the lower stub sill like the tank cars tested in the FRA reports. Similar high stress concentration near the interface between the head brace and the tank shell was observed in both cases. In the modified case 6, there is no plastic strain in lower stub sill, with a slight surpassing of the yield strength leading to some minor localized plastic strain at the interface between the head brace and the tank shell, where high stress is expected and cracks are likely to be found.

(a) [24]

(b) [10]

Figure 20: The pictures of the tested stub sill in the FRA reports that show only one slot in the stub sill

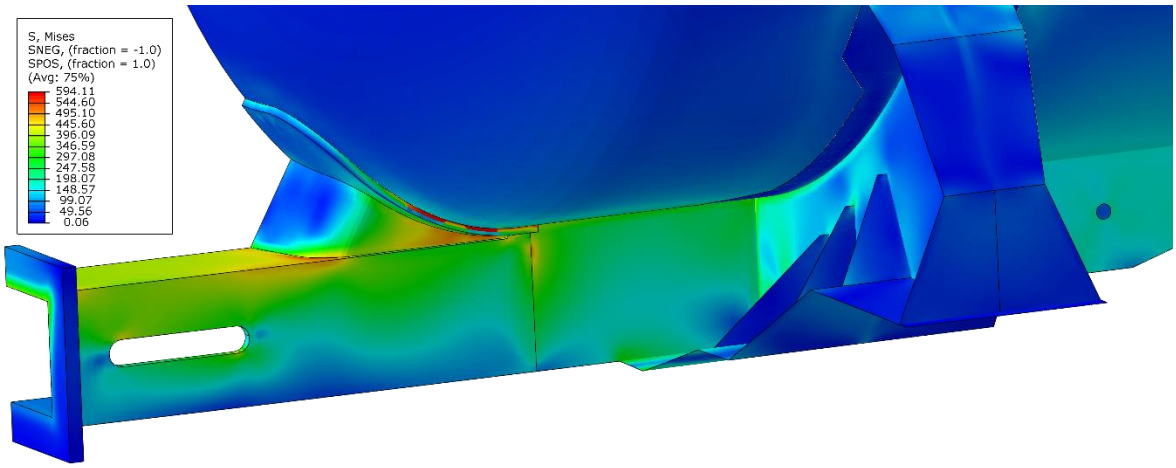

(a)

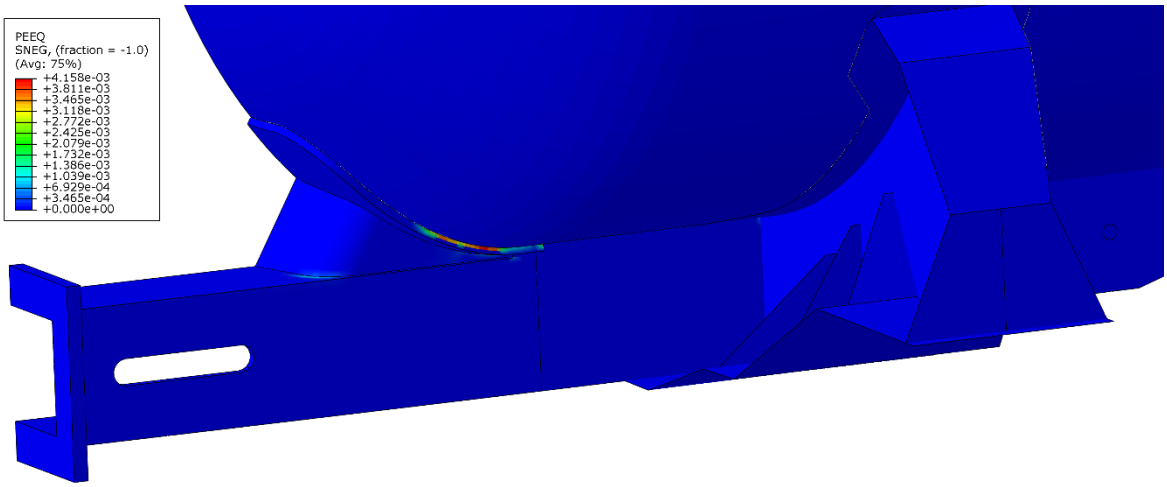

(b)

Figure 21: Distribution of Von Mises stress (a) and equivalent plastic strain (b) for the modified case 6 with no slots in the lower stub sill

The results of the eight cases studied are summarized in Table 4 below by peak stress and strain in the stub sill. Stresses that occur around the lower slot are not included. Note that the design load of the tank car is 1000 kips[1] and therefore small localized plastic strain above that load is not unexpected. No case below 1000 kips developed plastic strain. The strains that are seen are very small and localized. None of the cases experienced damage initiation. There is no indication

[1] AAR specification M-1001 contains the standards and recommended practices for the design and construction of freight cars for interchange service within the United States. Section 11.3.3.1 gives the requirement for testing to demonstrate that the structure of a freight car can successfully support a 1,000,000 pound compressive load (1000 kips) placed along its centerline of draft without experiencing permanent deformation. Additional requirements apply specifically to tank cars, and are given in M-1001 and M-1002.

that a single hard coupling event at these velocities (6-10 mph) would result in damage to a previously undamaged tank car.

Table 4: Peak stub sill stress and strain from impact scenarios

Scenario	Hammer Car	Target Speed	Peak load (CMAT calculation)	Peak Mises stress (MPa)	Peak Max. Principal strain	Plastic strain PEEQ
1	Empty	9.66 kph / 6 mph	3733 kN / 839 kips	382	9.9e-4	None
2	Empty	16.09 kph / 7.5 mph	7980 kN / 1793 kips	601	4.05e-3	3.27e-3
3	Partially Full	9.66 kph / 6 mph	4845 kN / 1089 kips	487	1.28e-3	3.82e-5
4	Partially Full	16.09 kph / 7.5 mph	9476 kN / 2130 kips	637	6.4e-3	6.17e-3
5	Full	9.66 kph / 6 mph	2286 kN / 514 kips	230	7.92e-4	None
6	Full	16.09 kph / 7.5 mph	6427 kN / 1445 kips	560	2.15e-3	1.2e-3
7 *	Full	9.66 kph / 6 mph	2511 kN / 565 kips	254	8.98e-4	None
8 *	Full	16.09 kph / 7.5 mph	9178 kN / 2063 kips	587	6.63e-3	6.53e-3

* Cases 7 and 8 use a twin pack draft gear while all other cases presented use steel friction

The peak loads listed in Table 4 are from CMAT's calculations based on the recorded strain. The listed coupling speeds are target speeds which may differ from the actual coupling speeds. This information is not currently available. The variability of the hard coupling test data is generally high as shown in Figure 1 earlier in this report. The limited test data provided to CMAT are near the top of the expected range for peak force. Some of the cases have higher than 1500 kips coupling forces, which are some of the worst cases shown in Figure 1.

In Figure 22, the coupling force of the limited cases investigated in this research is compared the averaged values from the FRA report. The two curves are the regression lines for each draft gear type from Figure 1. The point are the cases shown in Table 4. The coupling force data points investigated in this report are quite scattered and generally much higher than the averaged values. If damage had been seen in these aggressive cases CMAT would have run cases scaled to the average peak force for the impact velocity.

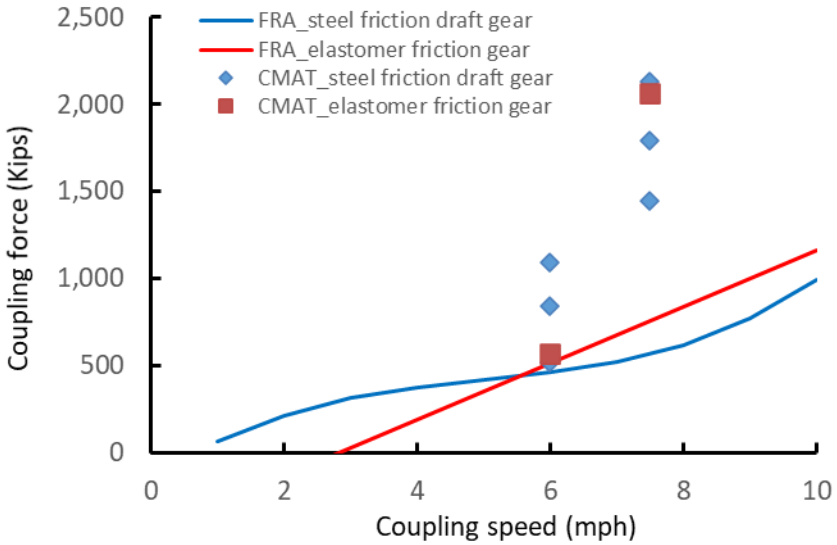

Figure 22: Comparison of the coupling force of the limited cases investigated in this research and the averaged value in the FRA report

Please note that these analyses are based on the assumptions that 1) the tank car is operated at room temperature, when the failure mode is ductile fracture, and 2) the stub sill is in perfect condition with no embedded flaws in the structure. The effect of low temperature and embedded flaws is preliminarily investigated in the following sections.

2.5 Preliminary FE analysis at low temperature

The strain-based damage mechanics model is used to simulate ductile fracture at room temperature. The failure mode transitions to brittle fracture at lower temperatures as described in section 1.4. To simulate this transition at low temperatures, a stress-based brittle fracture criterion was developed. Two modelling approaches, the explicit analysis utilizing subroutine VUMAT (a user defined material model) and the implicit approach using subroutine USDFLD (user defined failure), were developed to implement brittle failure criteria in the model. In both approaches, the maximum principal stress in the model was monitored and compared with the material strength.

The peak stress and strains from the low temperature simulations (-40°C) are compared to the 24°C simulations in Table 5 below. The stresses are slightly higher and the strains are slightly lower across the board. This occurs because the lower temperature material is slightly stiffer (higher modulus). No damage initiation occurred in any cases.

The material information presented earlier in the report demonstrates that TC128B and A572 Gr. 50 are more brittle (prone to fracture) at lower temperatures. However, the results of the FE simulations do not show increased failure at low temperature at the velocities studied (6 and 10 mph). The reason for this is that a clear stress concentration is required in addition to low temperatures for the brittle behaviour to occur. Preliminary work on embedded flaws is presented in the next section for this reason.

Table 5: Peak stub sill stress and strain from impact scenarios comparison between low temperature and moderate temperature

Scenarios	Peak load	Peak Mises stress (MPa) (24°C/-40 °C)	Peak Max. Principal strain (24°C/-40 °C)	Plastic strain PEEQ (24°C/-40 °C)
1	3733 kN / 839 kips	382/382	9.90e-4/9.79e-4	None/None
2	7980 kN / 1793 kips	601/639	4.05e-3/3.41e-3	3.27e-3/2.40e-3
3	4845 kN / 1089 kips	487/490	1.28e-3/1.26e-3	3.82e-5/8.83e-6
4	9476 kN / 2130 kips	637/678	6.4e-3/5.49e-3	6.17e-3/4.92e-3
5	2286 kN / 514 kips	230/230	7.92e-4/7.73e-4	None/None
6	6427 kN / 1445 kips	560/597	2.15e-3/1.85e-3	1.2e-3/7.20e-4
7	2511 kN / 565 kips	254/254	8.98e-4/8.88e-4	None/None
8	9178 kN / 2063 kips	587/605	6.63e-3/5.70e-3	6.53e-3/5.26e-3

The simulation of case 6 at –40 °C is rerun with user subroutine USDFLD. The effect of low temperature on the elastic and plastic properties of TC128B is not significant. Figure 23 shows that predicted strain at room temperature and low temperature of –40 °C are almost identical.

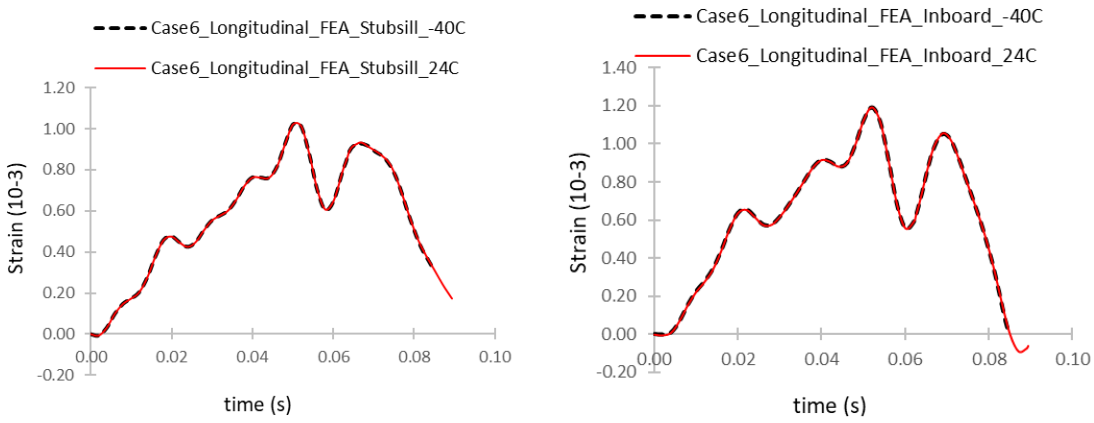

(a) (b)

Figure 23: Comparison of predicted strain at room temperature and low temperature for case 6.

The user defined variable SDV9, which is the maximum principal stress divided by the allowable strength, is plotted in Figure 24. In this case, the maximum allowable strength is 1425 MPa at -40 °C. The value of 1425 MPa at -40 °C was based on a conservative engineering judgement for the allowable level of stress for brittle failure at a stress concentration. The corresponding stress value at a sharp crack in the Charpy simulations was much higher with a value 2200 MPa [16]. The simulation predicted that the tank car is considered safe even at low temperatures and brittle fracture mode is assumed. The two materials TC128B and A572 have similar elastic-plastic properties prior damage, using only TC129B for the finite element model should be sufficient for the current research since no damage was observed.

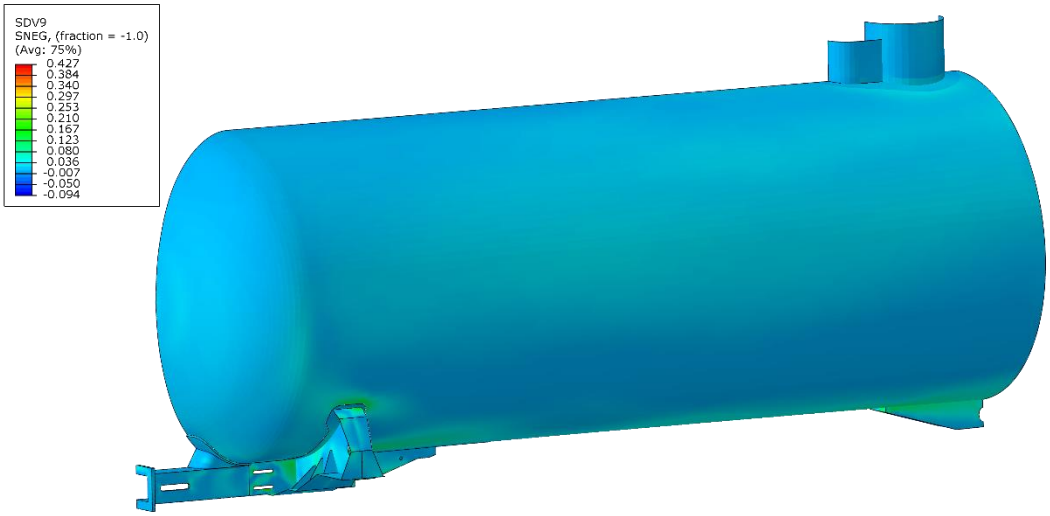

Figure 24: Plot of ratio of maximum principal stress and strength for tank car at low temperature

2.6 Preliminary FE analysis with embedded flaws

The results presented previously show that no damage is expected during hard coupling of a stub sill. A preliminary FE analysis study was conducted to investigate the effect of embedded flaws using the Extended finite element method (XFEM). An embedded flaw represents a discontinuity that results in a stress concentration or weakens the material. Potential sources of flaws in stub sills include: Manufacturing flaws such as voids that were small and below the threshold for detection of previous inspections; A fatigue crack due to cyclic loading; Environmentally assisted fracture. With XFEM, an unmeshed part can be used to cut the sub model of the stub sill to simulate the presence of embedded flaws. The embedded flaws can be moved around with no need to re-mesh the stub sill model. In this preliminary FE analysis study, only one flaw was embedded in the model, but multiple flaws can be implemented if needed.

In the hard coupling tests performed by FRA, no significant vertical load was recorded in the experimental condition. However, in realistic scenarios, the vertical load could be caused by the mismatch of couplers. In this preliminary FE analysis, the coupler force from Case #6 was modified to be used as boundary conditions. Figure 25 shows that an additional 20% of the longitudinal load based on Case #6 was applied in downward vertical direction. Longitudinal coupler forces during hard coupling produce predominantly compressive stress in the stub sill. Vertical forces, such as those caused by coupler miss match, are more likely to produce tensile stresses. Compressive stresses tend to close cracks which does not cause them to propagate. Tensile stresses open cracks leading to propagation. Longitudinal and vertical forces will both result in shear stress in welds between the stub sill and the shell. Shear stresses also lead to crack propagation.

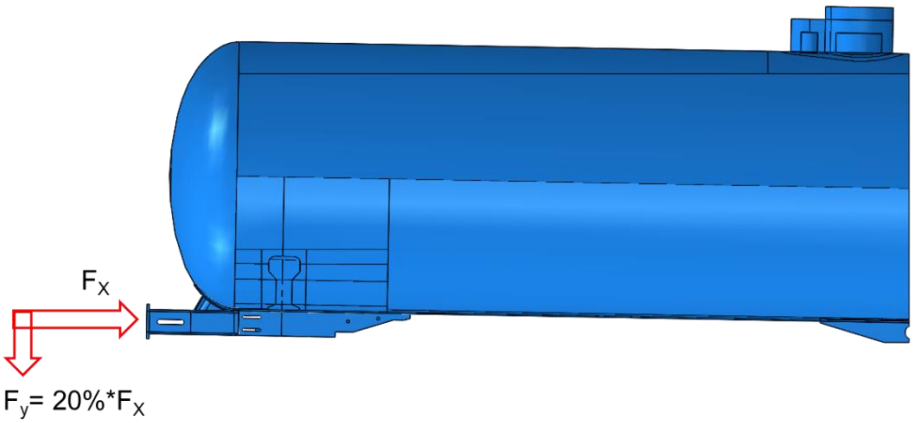

Figure 25: Downward vertical coupler force applied in the global finite element model

A circular shaped flaw with a diameter of 10 mm was inserted in the sub model of the stub sill, as shown in Figure 26. Any size, shape and orientation can be used for the embedded flaw, without the need for a complex mesh. This is a key benefit of the XFEM technique over traditional fracture mechanics. This preliminary FE analysis used arbitrary crack size, shape and orientation. The precise shape, size and orientation of embedded flaws should be determined based on actual observation in the future research.

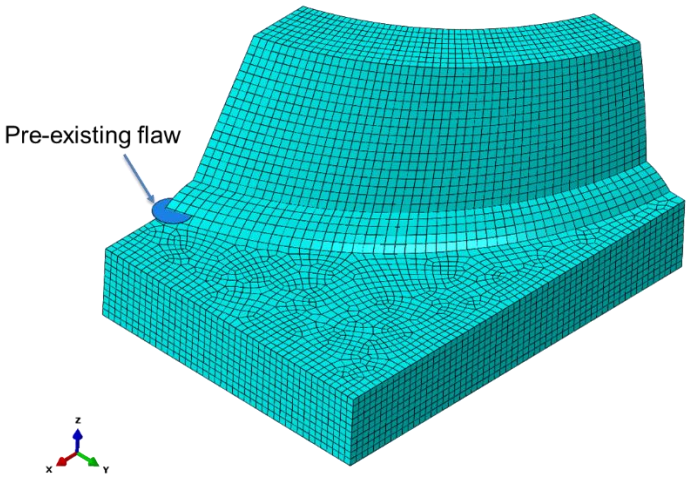

Figure 26: The sub model of the stub sill with a pre-existing flaw

The stress distribution of the stub sill with an embedded a flaw is shown in Figure 27. The downward vertical load cause tensile stress in some part of the stub sill and the embedded flaw could open at the moment of hard coupling. The embedded flaw in the stub sill could cause significant stress concentration at the crack tip depending on the location and sizes of the flaws.

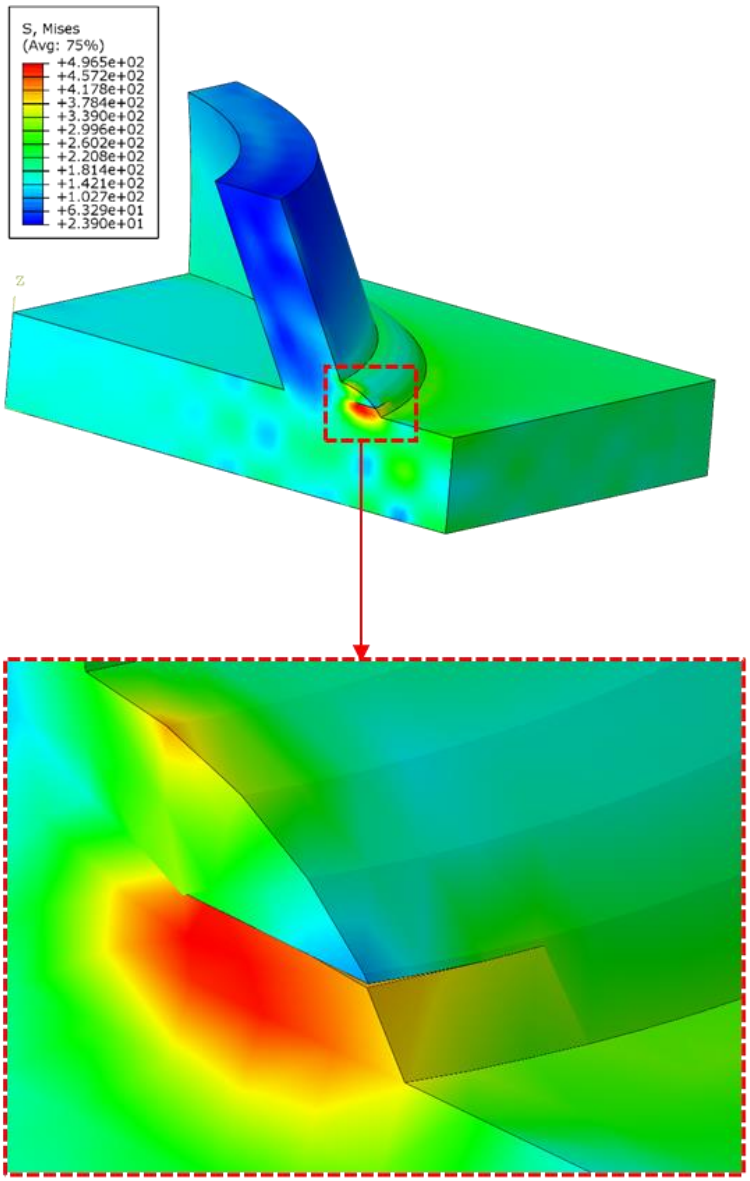

Figure 27: Crack opening in the sub modeling of tank car stub sill with embedded flaw

The XFEM coupled with the sub modelling method is found to be a good approach to investigate the effect of embedded flaws. Detailed FE analysis of the effect of crack location and critical crack size is recommended for future research.

3 EXPERIMENTAL STUDY OF A572-50

Tank car stub sills are made of several materials with A572-50 being the most common [25]. Some stub sills are made of TC129B. At the time of initiating this work CMAT had significantly more experience and experimental data of TC128B than A572-50. It would be time consuming and expensive to complete to repeat the experiments that have been already completed on TC128B for A572-50. Therefore CMAT and TC decided to begin simulations using TC128B models while a limited experimental study was conducted. The objective of this section is to compare the mechanical properties of A572-50 to TC128B and determine whether the existing models for TC128B can be adapted or whether additional testing should be conducted.

The objective of this task is to characterize A572-50 mechanical properties for accurate modelling and comparison with other common tank car steels, notably TC128B.

ASTM A572 is a high strength, low alloy steel plate that offers a combination of strength, weldability and economy. A572 Grade 50 is the most common grade and has the minimum yield strength of 345 MPa (50 ksi) which is the same as the AAR specification for TC128B. A572 Grade 50 Type 2 steel is used in tank car stub sill application. A572 steel is commonly used in as-rolled condition while TC128B is used in normalization heat treated condition. CMAT has used available material data for TC128B throughout this report. Tensile and Charpy testing was completed on A572-50 to determine whether the steel requires a separate model to be represented accurately. The composition of the A572-50 (commercial ASTM A572 Grade 50 Type 2 steel in as-rolled condition) and TC128B samples used in CMAT's testing are shown in Table 6.

Table 6: Comparison between composition of TC128B and A572-50. TC128B data is from Leco and atomic spectrography conducted at CMAT. A572 data is from the Mill test report.

Composition (wt%)		
	TC128B	**A572-50**
C	0.21	0.17
Si	0.34	0.27
Mn	0.97	1.3
Cr	0.039	0.11
Ni	0.0237	0.1
Mo	0.0133	0.001
Cu	0.0663	0.28
Al	0.0333	0.039
Nb	<.001	0.001
V	0.0019	0.028
Ti	0.0031	0.001
Sn	0.0048	N/A
B	0.0019	N/A
P	0.0033	0.014
S	<.001	0.007
Zr	<.005	N/A
Ca	0.0034	N/A
O	0.0035	N/A
N	0.0048	0.009

3.1 Tensile Testing

The tensile test matrix is shown in Table 7. Tensile properties of A572 Grade 50 Type 2 steel were similar to those of TC128B steel as shown in Table 8.The elongation of the A572 was lower than that of TC128B and it has a shorter discontinuous yielding region (up to 1.6% strain for A572 and 2.4% strain for TC128B) as shown in Figure 28. The difference between the two materials was likely due to different heat treatments (as-rolled vs. normalized). Tensile tests were carried out according to ASTM standard E8 and the impact experiments followed ASTM E23 for notched bar impact experiments.

Table 7: A572-50 test matrix

Test	**Specimen Orientation**	**Temperature (°C)**	**Speed (ASTM Test Standard)**
Tensile	RD	RT, -40	Quasi-static (E8)
	TD	RT	
Charpy	RD	RT, -20, -34, -46, -60, -80	Impact (E23)
	RD	RT, -34°C	Slow
	TD	RT	Impact (E23)
RD: Rolling direction TD: Transverse direction RT: Room temperature (23 °C)			

Table 8: A572-50 Tensile Test Results

Specimen	**T (◦C)**	**YS (MPa)**	**UTS (MPa)**	**E.L. (%)**	**R.A. (%)**	**Uniform E.L. (%)**
RD1	23	407	566	34.6	71.0	15.1
RD2	23	406	567	35.5	70.6	17.3
RD3	23	406	568	34.3	70.9	15.9
RD Avg.	**23**	**406**	**567**	**34.8**	**70.8**	**16.1**
RD4	-40	437	622	35.8	72.0	17.1
RD5	-40	457	626	35.0	70.8	15.8
RD6	-40	445	627	34.6	70.6	15.8
RD Avg.	**-40**	**446**	**625**	**35.2**	**71.1**	**16.2**
TD1	23	422	574	37.3	67.1	14.9
TD2	23	415	572	32.5	67.9	17.1
TD3	23	412	571	31.2	64.8	14.8
TD Avg.	**23**	**416**	**572**	**33.7**	**66.6**	**15.6**

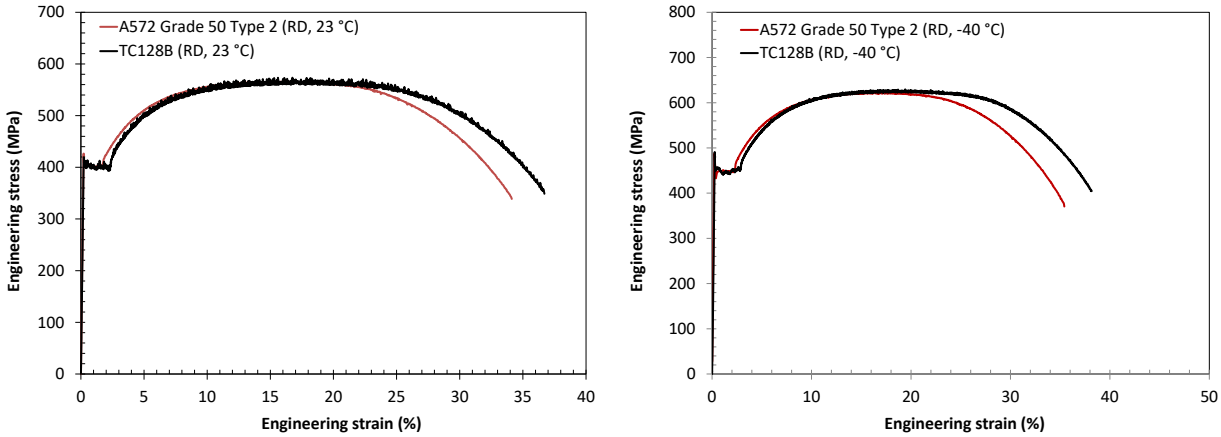

a) b)

Figure 28: Comparison of A572 tensile curve to TC128B at 23°C (a) and -40°C (b).

3.2 Charpy Absorbed Energy (CVN)

The Charpy test results for A572 are summarized in Table 9. CVN of the rolling direction were higher than those of transverse direction. The CVN values of A572 are lower than those of TC128B as is shown in the transition curves in Figure 29. This is considered due to the normalization treatment received by TC128B. Sudden load drops are usually associated to brittle fracture after some ductile fracture extension. This is seen on the fracture surfaces of broken A572 specimens.

Table 9: Charpy Absorbed Energy (CVN) of A572-50

T (°C)	**CVN (J)**	
	RD	TD
25	174 (177,183,163)	103 (108,98,102)
-20	118 (122,123,108)	-
-34	92 (82,97,97)	-
-46	59 (60,57,60)	-
-60	14 (9.4,22,11)	-
-80	10 (6.4,13,11)	-

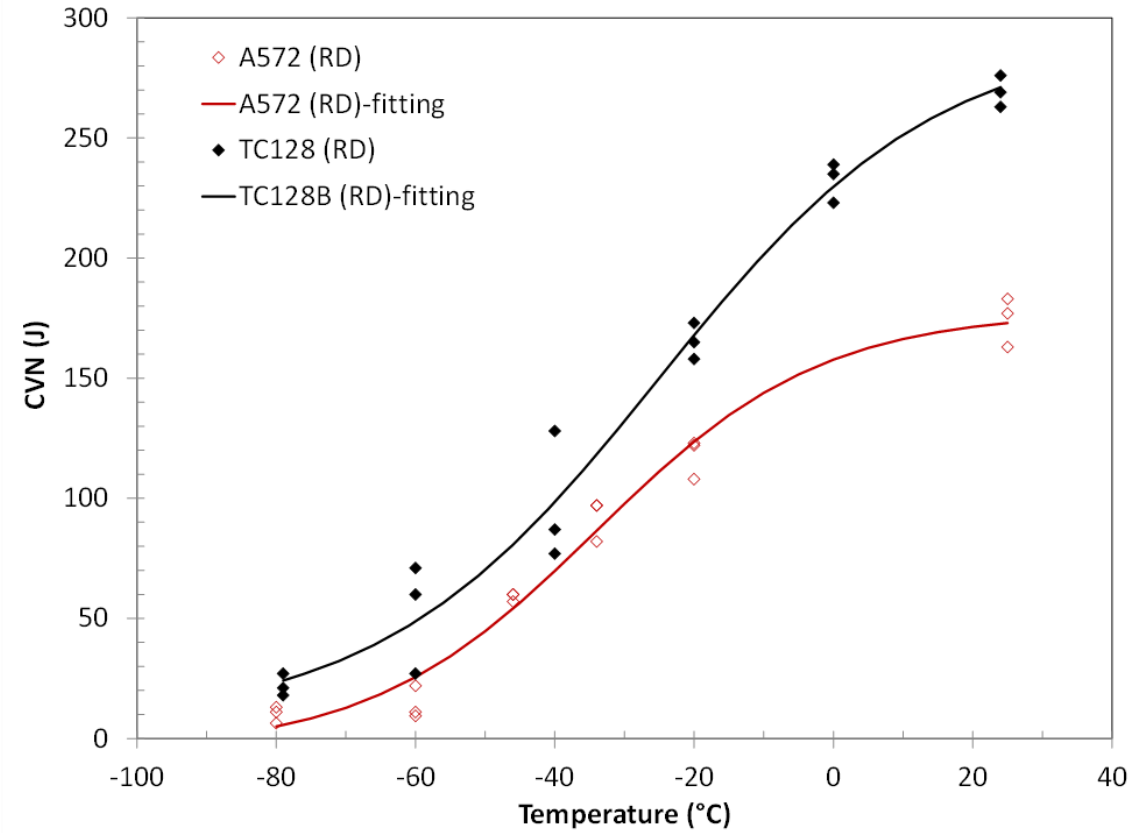

Figure 29: Comparison of rolling direction A572 and TC128B Charpy transition curves.

Non-standard quasi-static tests were performed on Charpy specimens using the fixture shown in Figure 30. The static Charpy test fixture used in this research and results are shown in Figure 31 and Figure 32 respectively. At 24 °C, increase of loading rate increased loads and energy absorbed. Specimens at impact and slow rates displayed load drops after deflections beyond approximately 10 mm.

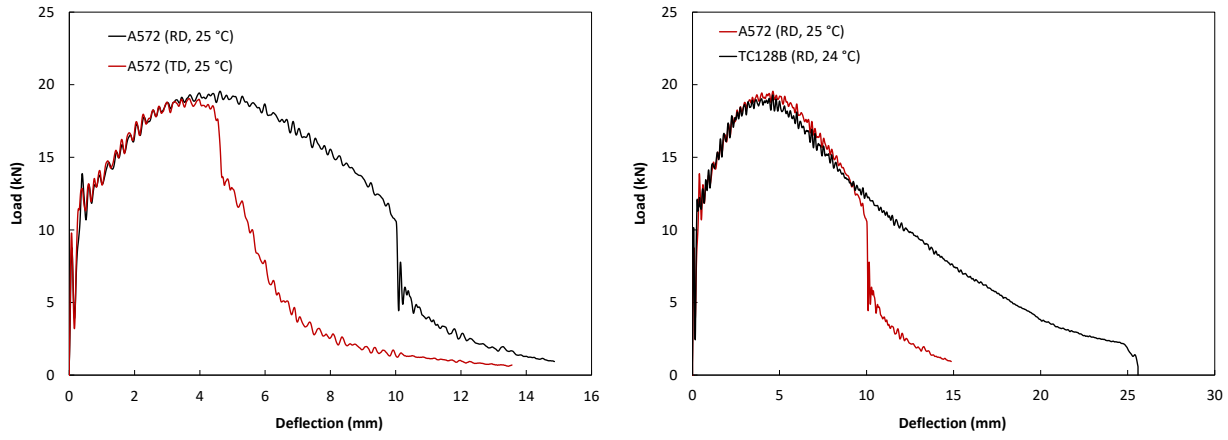

a) b)

Figure 30: Load versus displacement curves for showing (a) the difference between transverse and rolling direction CVN and (b) the difference between A572 and TC128B

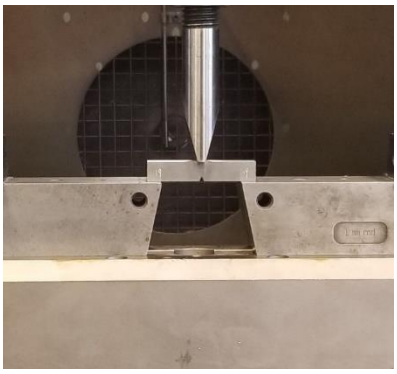

Figure 31: Static Charpy Sample Test fixture

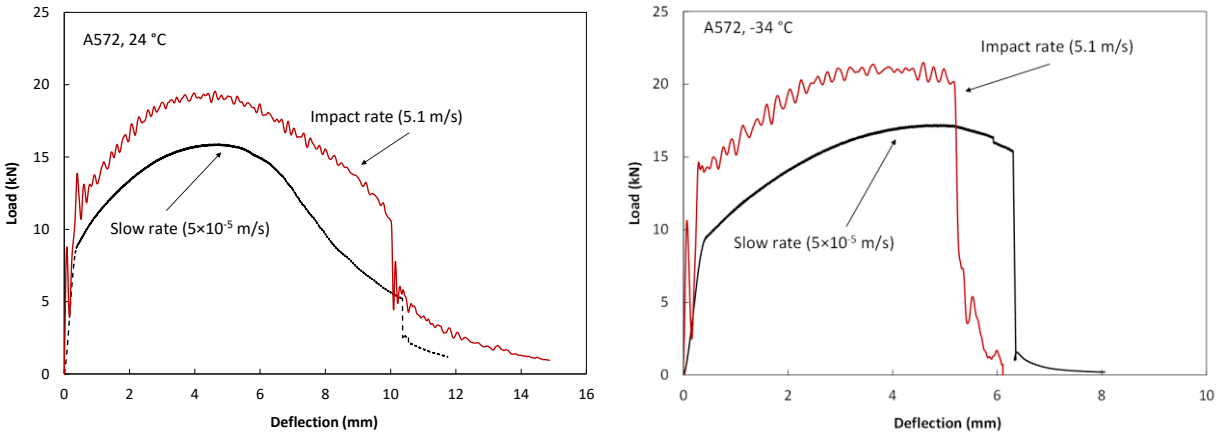

a) b)

Figure 32: Standard Charpy test load versus deflection curves and static Charpy curves.

The results presented here clearly show that A572 is brittle compared to TC128B. Analysis of hard coupling should be based on the worst case, or lowest performing material. Previous work by CMAT (Table 10, Figure 33) has shown that weld material is significantly more brittle than the base metal at low temperatures. At -34 C A572 has a CVN that is about 10% lower than TC128B while the weld material is almost 80% lower. Therefore it is likely that the welds connecting the stub sill and the tank are brittle. This is precisely the area that sees high levels of stress and in-service cracks. The FE model detailed in Section 3.2 considers a failure model with a ductile-brittle load response (for TC128B at -40 °C) that is representative of a brittle failure scenario. Future work should consider a failure model based on the TC128B weld material.

Table 10: Charpy absorbed energy (CVN) of TC128B circumferential weld: average (and individual)

T (°C)	CVN (J)	
	WM	HAZ
25	80 (102,69,69)	208 (232,145,248)
-20	26 (20,28,30)	109 (159,92,75)
-34	21 (29,13,24,20,19,20)	*
-46	18 (16,24,13)	32 (16,17,64)
-60	9 (10,9,9)	92 (120,142,152,66,16,53)
-80	6 (5,7,5)	21 (25,33,6)

* The HAZ was not tested at -34 °C.

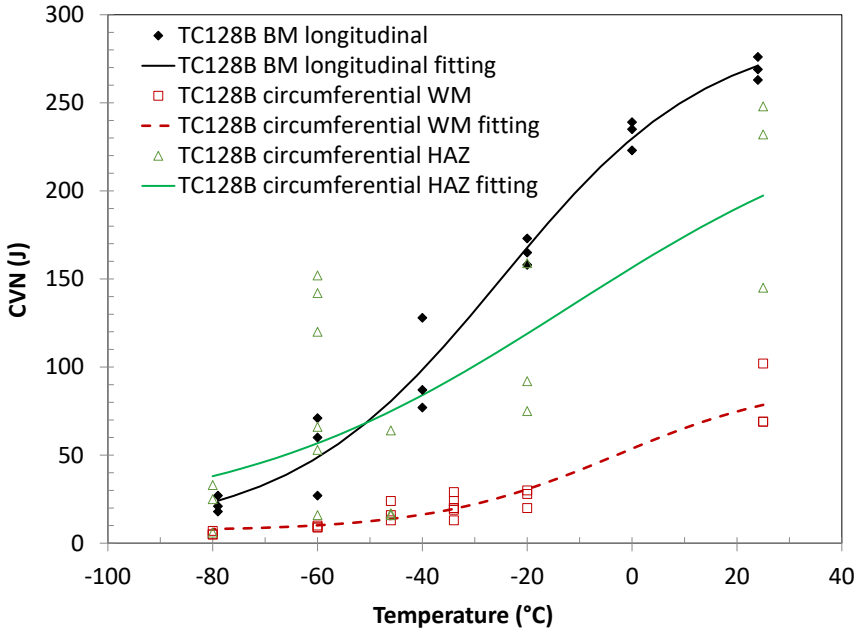

Figure 33 Charpy transition curve of TC128B BM, circumferential WM and HAZ.

3.3 A Note on Fatigue

This work focuses on the effect of a single hard-coupling event and therefore does not include fatigue analysis. For reference, information on the fatigue properties of tank car steels was sought. Alex Molina *et. al* [26] published the paper "Weibull S-N Fatigue Strength Curve Analysis for A572 Gr. 50 Steel, based on the True Stress-True Strain Approach" which included a S-N curve for A572-50. The data published included the ultimate tensile strength, $S_{ut} = 450.22\ MPa$, the yield stress, $S_y = 344.73\ MPa$ and the endurance limit of $S_e = 131.72\ MPa$. The yield and UTS values published were lower than CMAT's results. The yield stress was very close to the specification for the material of 345 MPa. The fatigue, or endurance limit, of 131.7 MPa is well below the yield stress.

4 CONCLUSIONS AND RECOMMENDATIONS

A full-scale tank car FE model was developed and used to simulate hard coupling impact. The material model used in the FE model was based on extensive testing of TC128B that was conducted in previous research at various temperatures and strain-rates. This analysis is based on the assumption that the stub sill is in an ideal perfect condition with no embedded flaws in the structure.

A few key achievements of this research are:

(1) Hard coupling test results from FRA were used to calibrate and validate the FE model. FE analysis results correlate very well with the test results.
(2) The two-step analysis, whereby a coarse mesh used in full-scale simulations is followed by a sub-model using a fine mesh to study regions of high stress, is found to be an accurate and very efficient modelling strategy. This lays the foundation for future research.
(3) In the worst scenario tested by FRA (10 mph, full on full, steel friction draft gear), the recorded peak load is 1500 kips and no significant plastic deformation and damage was observed in the FE analysis at both ambient temperature and low temperature (-40 ^{o}C). Section 10.7 of the *Transportation of Dangerous Goods Regulations* limit coupling speeds to below 9.5 mph (15.3 kph), which is below the speed simulated here.
(4) Locations of high stress concentration were identified in the FE analysis, such as near the interface between the head brace and the tank shell, and can be very helpful for damage tolerance analysis (allowable crack size).
(5) Sudden failure associated with brittle, or cleavage, fracture was not predicted at –40 °C for the conditions studied. However, consideration should be given to the possibility of a sudden loss of load bearing capacity under more aggressive conditions at low temperature.
(6) Limited material property testing was done on a common stub sill material, A572 to compare against TC128B. While TC128B performs better, the difference is not significant for the current modelling objectives. At -34 °C, A572 has a CVN that is approximately 10% lower than TC128B, while TC 128B weld material is almost 80% lower. It is therefore recommended that future testing of A572 and TC128B should focus on welds.

Only minor plastic displacement and no damage initiation was found in the scenarios investigated in this research. As the FE model was developed to capture crack initiation and propagation, more aggressive loading conditions on the full-scale tank car can be explored in future research. This includes studying the influence of offset loading and embedded flaws. For instance, the vertical coupling force which may result from a coupler mismatch is also found to be important, which could cause the embedded flaws to open in the event of hard coupling. Additionally, the failure model employed in FE was based on TC128B. Future work should consider a failure model based on the TC128B weld material, as it has been shown that TC128B weld material fails at much lower energy than TC128B at cold temperatures.

The existing regulations for tank car hard coupling restrict impact speeds with the intention of preventing damage to stub sills. Impact speeds are further reduced at low temperatures to address brittle material behavior. The most recent experimental work by the FRA supports the theory that impact force and therefore stress is proportional to impact speed. Therefore, limiting impact speed is a valid approach. The material testing conducted by CMAT on common tank car materials TC128B and A572-50 demonstrates that the material's static strength increases at lower

temperatures however its toughness, as measured by CVN, decreases. This decrease in toughness supports the reduction of allowable impact speeds. However when CMAT ran FE simulations of hard coupling at low temperatures damage due to brittle material failure did not occur for TC128B. Toughness is the measure of a materials resistance to cracking. For damage to occur, as seen in the Charpy samples tested, a sharp stress concentration is required in addition to low temperatures. It was also found that since hard coupling loads result in primarily compressive stresses in the stub sill and thus it is an unlikely driver of cracking.

Possible contributors to stub sill failures that should be considered for future work are:

(1) Pre-existing flaws (from manufacturing, fatigue, or other scenarios) may create the conditions for brittle fracture. If critical crack sizes have not been established for tank cars they should be investigated.
(2) Lower intensity but more frequent oscillating stresses (fatigue) may also be significant.
(3) Brittle behavior of weld material.

5 ACKNOWLEDGEMENTS

The authors would like to acknowledge many useful discussions with Kiran Shoib, Michael Spiess, Henry Lu and Ian Whittal of Transport Canada. Funding for this work was provided by Transport Canada's TDG Directorate.

6 REFERENCES

[1] Militaru D. Tank car stub sill analysis. National Research Council Canada; 1996.

[2] Miele CR, Rice RC. Stress Analysis of Stub Sill Tank Cars. Volpe National Transportation Systems Center. U.S. Department of Transportation, 1993.

[3] Cardinal JW, Mckeighan PC, Caldwell WN, Billing JR. Low Temperature Impact Effect on Tank Cars. National Research Council Canada; 2003.

[4] Carolan M, Rakoczy P. Side Impact Test and Analyses of a DOT-105 Tank Car. U.S. Department of Transportation; 2019.

[5] Tang YH, Yu H, Gordon JE, Jeong DY. Finite element analyses of railroad tank car head impacts. Am. Soc. Mech. Eng. Rail Transp. Div. RTD, 2009.

[6] González F. Full Scale Shell Impact Test of A DOT-117 Tank Car. U.S. Department of Transportation; 2018.

[7] Side Impact Test and Analyses of a DOT-111 Tank Car. 2015.

[8] Kirkpatrick SW. Detailed Puncture Analyses Tank Cars: Analysis of Different Impactor Threats and Impact Conditions. U.S. Department of Transportation; 2012.

[9] Gonzalez F. Yard impact test of a tank car. U.S. Department of Transportation, Federal Railroad Administration; 2019.

[10] Meymand S. Impact Test Data Analysis for Load Environment Characterization of Tank Car Stub Sill During Yard Operations. U.S. Department of Transportation, Federal Railroad Administration; 2020.

[11] Bai Y, Wierzbicki T. Application of extended Mohr-Coulomb criterion to ductile fracture. Int J Fract 2010;161:1–20. https://doi.org/10.1007/s10704-009-9422-8.

[12] Paredes M, Wierzbicki T, Zelenak P. Prediction of crack initiation and propagation in X70 pipeline steels. Eng Fract Mech 2016;168:92–111. https://doi.org/10.1016/j.engfracmech.2016.10.006.

[13] Paredes M, Sarzosa DFB, Savioli R, Wierzbicki T, Jeong DY, Tyrell DC. Ductile tearing analysis of TC128 tank car steel under mode I loading condition. Theor Appl Fract Mech 2018;96:658–75. https://doi.org/10.1016/j.tafmec.2017.10.006.

[14] Paredes M, Lian J, Wierzbicki T, Cristea ME, Münstermann S, Darcis P. Modeling of plasticity and fracture behavior of X65 steels: seam weld and seamless pipes. Int J Fract 2018;213:17–36. https://doi.org/10.1007/s10704-018-0303-x.

[15] BW Williams. Modelling the low temperature fracture response of TC128B. Research Result Report submitted to the Transportation of Dangerous Goods Scientific Research Division at Transport Canada, 2020.

[16] Williams BW, McKinley J, Xu S, Xue J, Spiess M. Capturing Variability in the Fracture Response of TC128B Steel using Damage Mechanics. Procedia Struct Integr 2020;28:1024–38. https://doi.org/10.1016/j.prostr.2020.11.118.

[17] Kirkpatrick SW, Ph D. Correlating Material Properties to Puncture Resistance to Enhance the Safety and Security of Tank Cars 2018.

[18] Rakoczy P, Gorhum T. Side Impact Test and Analyses of a DOT-117 Tank Car. US Department of Transportation Federal Railroad Association, 2019.

[19] Quick Calibration of Fracture Behaviors in TC128 Steel for Finite Element Modeling 2020.

[20] Abaqus users' documentation. https://www.3ds.com/products-services/simulia/services-support/support/documentation/, 2020.

[21] Kirkpatrick SW, Rakoczy P, MacNeill RA, Anderson A. Side Impact Test and Analyses of a DOT-111 Tank Car. U.S. Department of Transportation; 2015.

[22] González F. Full Scale Shell Impact Test of a DOT-105 Tank Car. U.S. Department of Transportation; 2018.

[23] Rakoczy P, Carolan M, Transportation Technology Center I, Center VNTS, Administration FR, Administration FR. Side Impact Test and Analysis of a DOT 112 Tank Car. 2016.

[24] Sundaram N, ENSCO I, Administration FR. Force Environment Evaluation of Stub Sills on Tank Cars Using Autonomous Over-the-Road Testing of the Instrumented Tank Car. 2016.

[25] S. Xu, Chen J, McKinley J, Liang J, Yang L, Laver A. Evaluation of Current Tank Car TC128B Steel Weld Performance. Report No. CMAT-2020-WF 49867504, 2021.

[26] Molina A, Piña-Monarrez MR, Barraza-Contreras JM. Weibull S-N fatigue strength curve analysis for A572 Gr. 50 steel, based on the true stress-true strain approach. Appl Sci 2020;10:1–12. https://doi.org/10.3390/app10165725.